Chapter 7
Modelling the Portevin-Le Chatelier Effect—A Study on Plastic Instabilities and Pattern Formation

Cristian Făciu

Dedicated to Academician Nicolae Cristescu on the occasion of his 87th birthday and to the 150th anniversary of the Romanian Academy.

7.1 Introduction

From macroscopic point of view the Portevin-Le Chatelier effect is an oscillatory plastic flow, resulting in inhomogeneous and discontinuous deformation that may be observed in metallic alloys subjected to load-or displacement-controlled experiments in a certain range of strain, strain-rate and temperature. From microscopic point of view the PLC effect is usually explained by a model called dynamic strain ageing (DSA) which characterizes the interaction between moving dislocations and between dislocations and diffusing solute atoms. The concept of DSA, first introduced by Cottrell and Bilby (1949) in the frame of the dislocation theory (see Cottrell 1953), generalized by Louat (1981) and later developed by others (see for instance Rizzi and Hähner 2004 and the references therein) is based on the pinning and unpinning of dislocations by impurity clouds.

In the present work, after reminding the main experimental and physical aspects of this phenomenon we introduce the principal ideas for incorporating the microstructural processes specific to the DSA into the phenomenological constitutive modelling. Our goal is to focus on macroscopic constitutive equations appropriate from the point of view of continuum mechanics. One way to realize this bridge from the microstructural aspects to the macroscopic mechanical behavior

C. Făciu (✉)
Simion Stoilow Institute of Mathematics of the Romanian Academy,
21 Calea Grivitei Street, 010702 Bucharest, Romania
e-mail: Cristian.Faciu@imar.ro
URL: http://www.imar.ro/∼cfaciu

D. Banabic (ed.), *Multiscale Modelling in Sheet Metal Forming*,
ESAFORM Bookseries on Material Forming,
DOI 10.1007/978-3-319-44070-5_7

associated with the PLC instabilities can be achieved by using the theory of flow localization due to the DSA proposed by McCormick (1988). In this framework, we survey the literature related with such macroscopic phenomenological approaches able to describe both the global responses, as observed typically in the stress-strain curves, but also the spontaneous appearance of strain localization.

In Sect. 7.2, following a line developed by Mesarovics (1995), Zhang et al. (2001), Böhlke et al. (2009) we give a detailed description of an elastic-viscoplastic model of McCormick type incorporating DSA and negative strain-rate sensitivity.

Starting from the idea that the PLC effect as well as all phenomena related with strain localization and band propagation are characterized by deformation which is inhomogeneous both in space and time, we consider that the appropriate framework for a phenomenological approach is the *field theory* approach. That means, in order to establish the predictions of a constitutive set of relations we have to add the general law of mechanics, for instance, the balance of momentum, the balance of mass and to investigate the resulting set of partial differential equations (PDEs) for initial-boundary value problems which simulate laboratory experiments.

In order to outline the basic ideas we consider for simplicity in Sect. 7.3 the case of a bar subjected to a one-dimensional stress state. We show that the field theory approach leads in this case to a hyperbolic semilinear PDEs system with source terms. The hyperbolic character of the system is due to the fact that we do not neglect the inertial term in the balance of momentum, although the PLC effect manifests only for strain-rate ranging between $10^{-6}\,s^{-1}$ and $10^{-2}\,s^{-1}$, which usually are considered as static tests.

We accurately formulate initial-boundary value problems corresponding to strain- and stress-controlled tests. Moreover, we do not add as usual a machine equation in order to describe the machine effect, but we formulate in a new way mixed stress- and strain-controlled boundary conditions which include a parameter describing the influence of the testing machine.

A numerical investigation of uniaxial tensile tests is done using an explicit finite difference scheme based on the method of characteristics described in Appendix. It is shown that, without introduction of a geometric defect or other heterogeneity, the PDEs system is able to describe quantitatively the remarkable features of the PLC effect, that is, the staircase response for a soft testing device, the jerky flow for the hard device depending on the imposed strain-rate, but also strain localization phenomena and pattern formation.

In the mathematical framework developed, we consider in Sect. 7.4.1 a spatial homogeneous process in stress, strain and ageing time, as the solution of an ideal initial-boundary value problem. That corresponds to a constant cross-head velocity controlled experiment having a linear distribution of the velocity in the bar at the initial moment. A linear stability analysis of this homogeneous solution allows to determine a critical condition on some material parameters for the PLC effect. Moreover, one determines the range of strain-rates and mechanical parameters for which there exists a jerky flow. One shows that the boundaries of the unstable PLC

domain correspond to a Hopf bifurcation with limit cycle behavior. Section 7.4.2 concerns the calibration and verification of the constitutive model.

7.1.1 Experimental and Physical Aspects

The phenomenon of discontinuous deformation in tensile tests had already been observed in the first part of the 19th century in dead weight tests. By adding successively weights to the end of copper strips, the French physicist Savart (1837) observed that the deformation does not increase continuously, but by sudden jumps, feature known now as "staircase" like stress-strain behavior. He was the first to consider this phenomenon as an intrinsic material property of plastic deformation. More careful and systematic tests have been considered by his student Masson (1841) who performed tests on different alloys at different temperatures. That is way sometimes this phenomenon is referred as Savart–Masson effect (see the historical comments in Bell (1973), Scott et al. (2000), Rizzi and Hähner (2004)). The use of "hard" testing machines, i.e. of strain-controlled experiments, at the beginning of 20th century, had allowed Portevin and Le Chatelier (1923) to investigate in a systematically manner the serrated yielding in aluminium alloys at different elongation rates and to definitively remove a common belief that such irregularities and discontinuous deformation are only a machine-produced effect of little importance. In recognition of their results, starting with the work of Cottrell (1953), this phenomenon of discontinuous deformation of metals, in quasi-static tests, bears their name.

Thus, the PLC effect is an unstable, irregular plastic flow resulting in an inhomogeneous deformation that may be observed in some dilute metallic alloys. These are, for example, steels and aluminium alloys which are important industrial materials used for car bodies, aircraft fuselage and different type of casing. The localized deformation associated with the PLC effect leads to the formation of narrow bands of intense plastic deformation that leaves undesirable traces on the surface of the final product. Moreover, it affects most materials properties *by increasing*: the flow stress, the ultimate tensile strength and the work hardening rate and *by decreasing*: the ductility of metals, the strain-rate sensitivity coefficient and the fracture toughness (see Yilmaz 2011).

From *macroscopic point of view* the PLC effect is characterized by the following aspects. In *constant strain-rate* tensile experiments, i.e. when the end of the test specimen is subjected to a constant velocity motion, the PLC effect appears in certain ranges of temperature and strain-rate and manifests by a discontinuous deformation, which corresponds to serrated stress - strain curves ("jerky flow"). The most distinct feature is the localization of strain in the form of visible bands, apparently moving along the surface of the specimen gauge. The apparition of each strain band corresponds to a burst of plastic activity.

While for most metallic alloys the stress-strain curves obtained in tensile tests moves up when the strain-rate increases, for the alloys which show the PLC effect the reverse phenomenon happens, that is, they move down. This behavior is known

as *negative strain-rate sensitivity* (NSRS) of the flow stress. It is illustrated in Fig. 7.1 where one can see that the highest strength and the highest stress-strain curve is obtained for the lowest strain-rate, i.e. for 6×10^{-4} s^{-1}. As the strain-rate increases to 6×10^{-3} s^{-1} and ultimately to 6×10^{-2} s^{-1} the two stress-strain curves are lower, thereby indicating a negative strain-rate effect. At constant strain-rate, the amplitude of the serrations increases gradually with strain and then finally saturates at large strains. Moreover, the amplitude of serrations decreases with increasing strain-rate.

Experimental observations have shown that different types of serrations correspond to different ways the PLC bands nucleate and move along the specimen leading finally to specific band patterns. These are designated as type A, type B and type C, serrations and correspondingly as type A, type B and type C, PLC bands (see for instance Chihab et al. 1987). They are illustrated in Fig. 7.2. The transition between *band types* or, equivalently, *serration types* may occur upon changes in strain-rate and temperature. Usually, higher strain-rates are associated with type A bands, lower strain-rates with type C bands and intermediate levels with type B bands.

Type C bands nucleate randomly and appear as hopping bands throughout the specimen gauge and the corresponding serrations have a relative constant amplitude and frequency. Type B bands propagate in a gauge in an intermittent manner with approximately equal intervals having amplitudes and frequencies somewhat irregular and smaller than those of a type C curve. Type A bands propagate apparently continuously in a gauge resembling a longitudinal wave (see Ait-Amokhtar and Fressengeas 2010), with arbitrarily located small stress drops embedded in the regular flow in the tensile test curve.

Different optical methods, laser scanning extensometry, infrared thermographic techniques, or digital image correlation methods, (see for instance Chihab et al. 1987; Neuhäuser et al. 2004; Ait-Amokhtar et al. 2008; Benallal et al. 2008a, b;

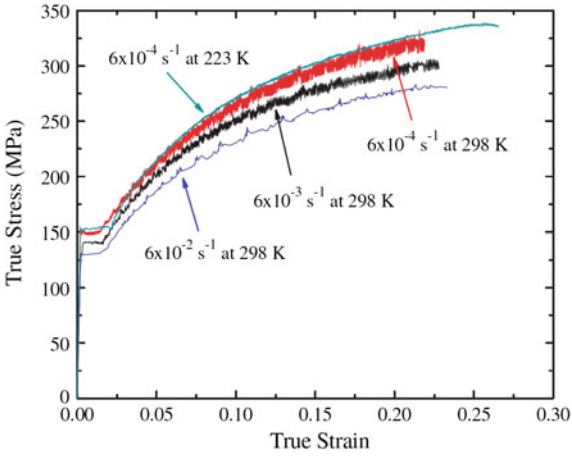

Fig. 7.1 True stress-strain curves of AA5754 alloy at various strain-rates and temperatures (reproduced with permission from Halim et al. 2007 Elsevier Ltd.)

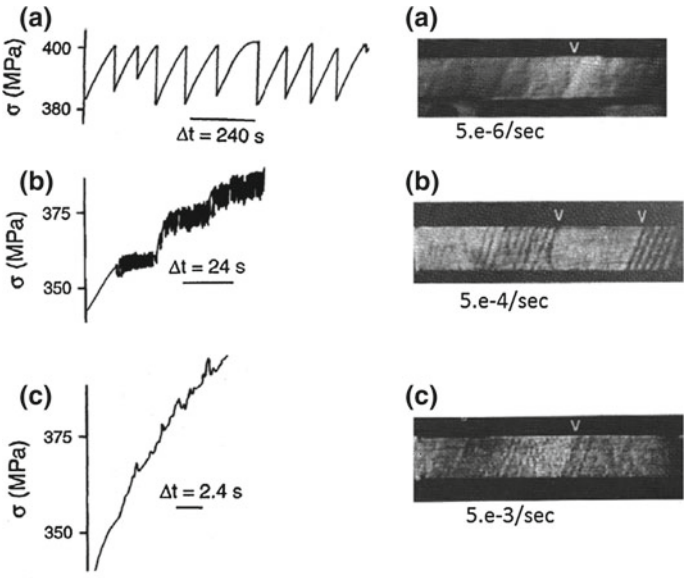

Fig. 7.2 Stress-time curves for an Al–Mg alloy at $T = 300\,^{\circ}\mathrm{K}$ showing the change from type C to type B, and then to type A serrations with increasing strain-rate. **a** Type C; $5 \times 10^{-6}\ \mathrm{s}^{-1}$, **b** type B; $5 \times 10^{-4}\ \mathrm{s}^{-1}$ and **c** type A; $5 \times 10^{-3}\ \mathrm{s}^{-1}$ (reproduced with permission from Chihab et al. (1987) and Yilmaz (2011) Elsevier Ltd.)

Zdunek et al. 2008; Ait-Amokhtar and Fressengeas 2010 and the references therein) have allowed to correlate the spatio-temporal characteristics of the PLC effect with the associated serrations observed in conventional tensile tests.

Thus, if one looks at a zoom of the "saw teeth" stress–strain curve of a constant strain-rate test (see Fig. 7.3) obtained using Digital Image Correlation technique by Zdunek et al. (2008) one observes that it is composed by a rapid stress drop followed by a slow reloading part and this process runs almost cyclically. One notes also that each stress drop accompanies a local dynamic event evidenced by the nucleation of a strain band and the subsequent strain band buildup (see the strain distribution in images 3–4 and 7–8). On the other side, when the stress increases quasistatically there is no strain nucleation and the bands remain unchanged (see the strain distribution in images 1–2 and 5–6). In this way, cyclic strain accumulation occurs leading to a strain pattern formation along the specimen. In other words, the plastic flow appears as "strain bursts-and-arrests" and the strain band propagation can be of type "go-and-stop".

The experimental effort on the PLC effect has been mainly devoted to constant strain-rate tests and the atypical load-extension curves obtained have led to the acceptance of the term "serrated flow" as a synonym for the expression "Portevin-Le Chatelier effect".

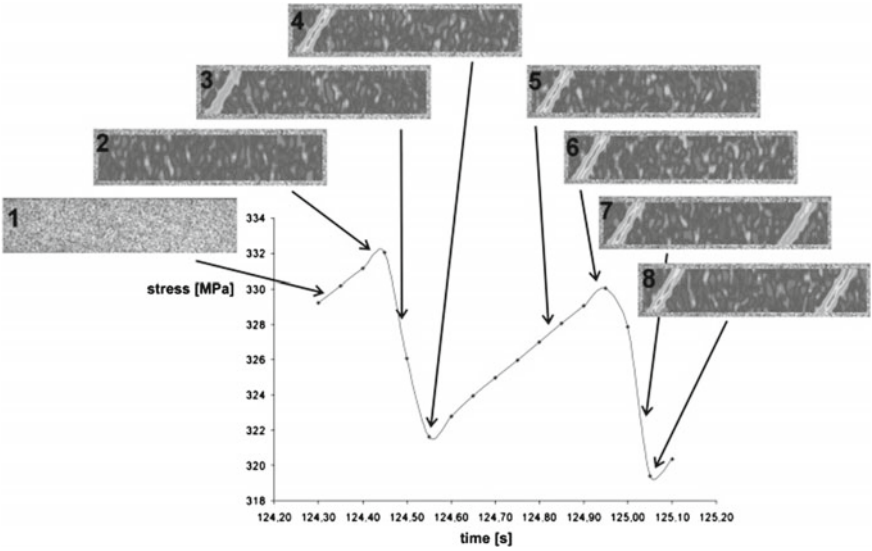

Fig. 7.3 Correlation between stress drops and pattern formation: strain band localization during a stress drop and no change in strain distribution during the stress increase (reproduced from Zdunek et al. (2008) Elsevier Ltd.)

Considerably less attention has been paid to *constant stress-rate* tests. In these experiments the PLC effect manifests by stress-strain curves which are no longer "serrated", but exhibit "staircase steps". As it is described by Fellner et al. (1991) there are two ways to conduct a constant-$\dot{\sigma}$ test. The first modality is to perform dead-load experiments using a creep machine by programmed addition of water, for example, which allow a careful control of the loading rate. This is a so-called dead-load tensile machine and the experiment is called a *true constant-$\dot{\sigma}$* test. In this case "almost perfect" steps can be obtained as it is illustrated in Fig. 7.4. The second way, but the most common in laboratory experiments, is to use a conventional tensile testing machine with electronic control systems. Such a machine is used as a hard testing machine for constant extension-rate tests, but when one inserts a spring of weak stiffness between the specimen and the grips of the machine it is used as a soft testing machine for constant loading-rate tests. In this case, the steps of the staircase present always a decrease of the stress and even successive "oscillations" (see Figs. 3–4 in Fellner et al. 1991). The machine effect on the "staircase shape" is not negligible as it can be seen from the physical experiments in Fig. 7.5 obtained using a Zwick testing machine equipped with digital recording. This experiment can be considered a *"pseudoconstant-$\dot{\sigma}$"* test.

It is important to note that, unlike the constant strain-rate tensile experiments in which the serrations on the stress-strain curves are accompanied by the appearance of visible localized deformations bands along the gauge length, in true constant stress-rate experiments no well defined stretcher-strain markings can be revealed on the surface of the specimen (Fellner et al. 1991).

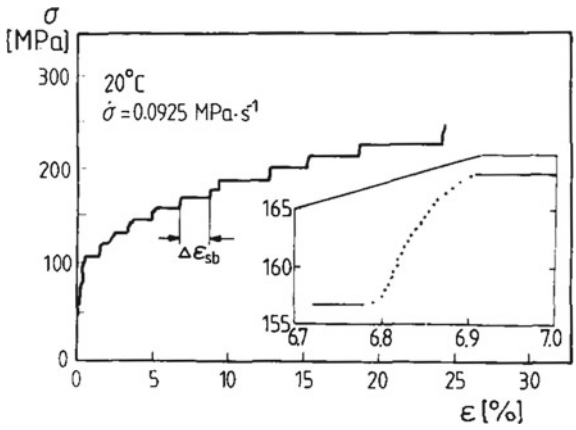

Fig. 7.4 Strain bursts in a dead-load tensile machine with constant stress-rate for annealed AlMg3 (reproduced from Fellner et al. (1991) Elsevier Ltd.)

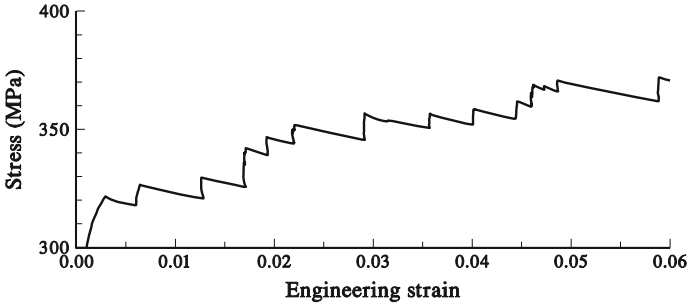

Fig. 7.5 Strain bursts in a Zwick testing machine in a nearly constant stress-rate test ≈ 0.076 MPa/s for a 5182H28 alloy (reproduced with permission from Făciu et al.1998 EDP Sciences)

However, Cuddy and Leslie (1972), testing several alloys of iron, by means of a creep tensile test machine, with an incrementally increased stress, have put into evidence that deformation bands can be detected by the oscilloscope traces of the outputs of a double extensometer. These bands spread immediately over the entire gauge length of the specimen while the stress remains constant and large strain increments are recorded.

More sophisticated experiments at constant stress-rate have been performed by Neuhäuser et al. (2004), Chmelík et al. (2007) using acoustic emission and laser extensometry techniques in order to detect the movement of a deformation band. It has been shown that the deformation band movement is characterized most appropriately by a repeated nucleation of bands. This appears as a piecewise continuous propagation at higher and strongly scattered values of propagation velocity as compared to the A-type in strain-rate controlled tests. They claim that "in fact there is a new generic type of PLC bands at the stress-rate controlled deformation".

From *microscopic point of view* the plastic flow in metals can be explained by using the theory of dislocations (see for instance Cottrell 1953; Nabarro 1967). In general, when dislocations move without interacting each other, or without interacting with point defects, the plastic flow is steady and stable. When the motion of dislocations is disturbed by different kind of interactions the plastic flow becomes unstable as it happens in the case of PLC effect. This phenomenon is usually explained by a model called *dynamic strain ageing* (DSA) which characterizes the interaction between moving dislocations and between dislocations and diffusing solute atoms (see Cottrell and Bilby 1949). It is considered that when the dislocations meet obstacles like solute atoms, or interstitial particles, they are temporary arrested for a certain time. If sufficient stress is applied these dislocations will overcome these obstacles and will quickly move to the next obstacle where they are stopped again and the process is repeated. This microscopic mechanism, referred to as dislocation pinning by solutes (Cottrell 1953), is believed to be the main factor controlling instabilities in plastic flow and in particularly the PLC effect. The dynamic strain ageing as micro mechanism of plastic instability phenomenon described by dislocation–solute and dislocation–dislocation interactions is in agreement with the experimental macroscopic correlation of the spatio-temporal characteristics of the PLC effect, obtained by different imaging techniques, as it is illustrated, for example, in Fig. 7.3. The idea of DSA has been further developed by van den Beukel (1975), Mulford and Kocks (1979), Louat (1981), McCormick (1988), Springer et al. (1998), Rizzi and Hähner (2004).

7.1.2 Main Ideas for the Constitutive Modelling of the PLC Effect

Phenomenological viscoplastic models used to describe the PLC effect are mainly based on two directions. One is motivated by the empirical material law adopted by Penning (1972) in his analysis of the tension tests for materials with negative strain-rate sensitivity. This relay on the assumption that in uniaxial tension, the stress σ is defined as a function of plastic strain ε^p and plastic strain-rate $\dot{\varepsilon}^p$ in the form

$$\sigma = \sigma_Y + \sigma_H(\varepsilon^p) + \sigma_V(\dot{\varepsilon}^p), \tag{7.1}$$

where σ_Y is the yield stress, σ_H is the strain hardening variable, and σ_V is the viscous stress governing the strain-rate sensitivity of the flow stress. It is assumed that the viscous stress is non-negative, but in order to include negative strain-rate sensitivity, σ_V is taken as a decreasing function of $\dot{\varepsilon}^p$ in a bounded region of the plastic strain-rate, i.e. there is a N-shaped relationship between the plastic strain-rate and flow stress. This model has been extended by Kubin and Estrin (1985) by adding the so-called "machine equation"

$$\frac{\sigma(t)}{M} = \frac{V^*}{L}t - \frac{1}{L}\int_0^L \varepsilon(x,t)\mathrm{d}x, \tag{7.2}$$

where M is the combined elastic modulus of the specimen and the testing machine, L is the length of the specimen and V^* is the imposed end velocity. This approach has led to a nonlinear integro differential system involving a spatial variable x and a temporal variable t which allowed to model constant stress-rate experiments. Penning's constitutive equation has been modified by Hähner (1993) by incorporating second order strain-gradients $\partial^2\varepsilon^p/\partial x^2$ to capture a spatial coupling of the PLC effect. A generalization of the material law (7.1) for a three dimensional viscoplastic model has been considered by Benallal et al. (2003, 2006).

The second direction is based on the constitutive relations introduced by McCormick (1988) to describe the dynamic strain ageing. The model assumes that the plastic flow occurs as a result of thermally activated escape of dislocations that have been pinned by solute atoms and can be described by an Arrhenius-type law. This implies that the plastic strain-rate $\dot{\varepsilon}^p$ is related to the stress σ and the average local solute concentration near dislocations C by relation

$$\dot{\varepsilon}^p = \dot{\varepsilon}_0 \exp\left(\frac{\sigma - \sigma_H(\varepsilon^p)}{S} - HC(t_a)\right) \Leftrightarrow \sigma = \sigma_H(\varepsilon^p) + SHC(t_a) + S\ln\left(\frac{\dot{\varepsilon}^p}{\dot{\varepsilon}_0}\right), \tag{7.3}$$

where $\dot{\varepsilon}_0$ is a characteristic strain-rate, S and H are material constants controlling the instantaneous and steady-state strain-rate sensitivity of the solid. Here $\sigma_H(\varepsilon^p)$ describes the stress hardening part of the flow stress. The solute concentration C, according to the original model proposed by Cottrell and Bilby (1949) and modified by Louat (1981), depends on average age of dislocations according to relation

$$C(t_a) = 1 - exp\left(-\left(\frac{t_a}{t_D}\right)^n\right), \tag{7.4}$$

where t_D is the characteristic time for solute diffusion across dislocations, n is a phenomenological material constant and t_a is the time that a representative mobile dislocation is pinned by obstacles. The age of dislocations t_a evolves according to a phenomenological kinetic law which will be described bellow.

An obvious inconvenience of the Arrhenius-type relation (7.3) is that when it is coupled with an elastic unloading condition, and σ is lower than the flow stress, it yields a finite plastic strain-rate (see Estrin 1996). Therefore, a different flow rule has been proposed by Böhlke et al. (2009), whereby the plastic strain-rate $\dot{\varepsilon}^p$ is related to the stress σ not by an exponential function as in (7.3), but by a power law, coupled with an unloading condition, i.e.

$$\dot{\varepsilon}^p = \dot{\varepsilon}_0\left(\frac{\sigma - \sigma_H(\varepsilon^p)}{S} - HC(t_a)\right)^m, \tag{7.5}$$

where $m > 0$ is a material constant which describes the strain-rate sensitivity of the material. By using this flow rule a geometrically non-linear elastic–viscoplastic constitutive model has been used for simulation of material response under various applied strain-rates.

For steady-state conditions the ageing time t_a may be taken to be equal to the *waiting time of dislocations*, t_w, as given by the Orowan equation, which relates the plastic strain-rate to dislocation densities and the average velocity of mobile dislocations, $v_D = \frac{l}{t_w}$, by relations

$$t_w = \frac{\rho_m b l}{\dot{\varepsilon}^p} = \frac{\rho_m b \rho_i^{-1/2}}{\dot{\varepsilon}^p} = \frac{\Omega}{\dot{\varepsilon}^p} \tag{7.6}$$

where ρ_m is the mobile dislocation density, ρ_i is the immobile dislocation density, l is the effective obstacle spacing, that is, the effective mean free path between obstacles, and b is the length of the Burgers vector. Ω is in fact the strain produced by all mobile dislocations moving to the next obstacle on their path. Since according to (7.6), Ω varies with the dislocation densities it follows that from phenomenological point of view it varies with the plastic strain, that is, $\Omega = \Omega(\varepsilon^p)$. The strain dependence of Ω can be calculated using a dislocation model (see Zhang et al. 2001) and taken as

$$\Omega = \omega_1 + \omega_2 (\varepsilon^p)^{\beta} \tag{7.7}$$

where ω_1, ω_2 and β are constants.

Relation (7.6) reflects the generally accepted fact that a decrease in plastic strain-rate causes an increase in the waiting time spent by dislocations at obstacles, which in turn will increase the magnitude of the stress drop in a jerky flow.

According to McCormick and Ling (1995), measurements of transient behavior following abrupt changes in $\dot{\varepsilon}^p$ or σ indicate that t_a is not an instantaneous function of $\dot{\varepsilon}^p$, but rather may be approximated by a first order relaxation kinetics law (see Ling and McCormick 1993). That means, the effective *ageing time* t_a is not identical to the average *waiting time* t_w a dislocation is arrested at localized obstacles. The fundamental assumption proposed by McCormick (1988) is that the effective ageing time t_a "relaxes" towards t_w with time t according to the evolution law

$$\frac{\mathrm{d}t_a}{\mathrm{d}t} = \frac{t_w - t_a}{\tau}, \tag{7.8}$$

where the characteristic relaxation time τ is taken to be equal to t_w.

Therefore, from (7.8) and (7.6) the age of dislocations t_a evolves with time, plastic strain and plastic strain-rate according to the phenomenological kinetic law

$$\frac{\mathrm{d}t_a}{\mathrm{d}t} = 1 - \frac{t_a}{t_w}, \quad \text{where} \quad t_w = \frac{\Omega(\varepsilon^p)}{\dot{\varepsilon}^p}. \tag{7.9}$$

Let us note that if $t_w \gg t_a$, then from (7.9) it follows that $\frac{\mathrm{d}t_a}{\mathrm{d}t} \cong 1$, in agreement with the fact that the solute concentration at arrested dislocations cannot increase faster than that allowed by the passage of time (McCormick 1988).

McCormick's model has been used in a large number of theoretical and numerical studies. It has been extended to the three-dimensional case by interpreting relation (7.3) as a relation between the von Mises equivalent deviatoric stress and the equivalent plastic strain. Analytical and numerical stability and bifurcation analysis have been done by Mesarovics (1995). There are several studies in the literature in which such kind of three-dimensional constitutive approaches have been investigated numerically by using the finite element method. The first numerical study in a 3D context has been done in McCormick and Ling (1995) by discretizing the tensile specimen into a number of axisymmetric sections and simultaneously solving the constitutive equations for dynamic strain ageing in each section. A reference approach is that in Zhang et al. (2001) where finite element simulations of dynamic strain ageing in flat and notably round specimens have been implemented by using the ABAQUS code. The model has been also used by Graff et al. (2004) and investigated in a finite element code for strain localization phenomena associated with static and dynamic strain ageing in notched specimens. In Jiang et al. (2007) a phenomenological model that includes spatial coupling is developed on the basis of McCormick's constitutive assumptions. In this case the specimen is numerically divided into N sections with equal width, perpendicular to the axial direction and coupled through the acting load. An experimental and numerical investigation of the PLC effect in the aluminium alloy AA5083-H116 was carried out by Benallal et al. (2008a) using the explicit non-linear finite element code LS-DYNA for different specimen geometries. In Zhang et al. (2012) a simple modification of McCormick's model has been made by introducing a power law dependence in the right part of Eq. $(7.9)_1$ to modify the transient kinetics of the strain-rate response of the material. Numerical simulations of PLC band formation and necking in a tensile specimen have been performed using the explicit dynamic finite element code ABAQUS. By using the flow rule (7.5), Böhlke et al. (2009) have considered a geometrically non-linear elastic-viscoplastic constitutive model for simulation of material response under various applied strain-rates. A related elastic-viscoplastic approach with that proposed by Böhlke et al. (2009) has been used by Mazière and Dierke (2012) to investigate the PLC critical strain in an aluminum alloy.

More complex constitutive laws derived from a depth analysis of physical mechanisms have been developed and are suitable, but more difficult to implement. For instance, Rizzi and Hähner (2004) have introduced two intrinsic time scales in the evolution equations and a characteristic length scale through a diffusion-like term with spatial second-order gradient. Soare and Curtin (2008a, b) have

developed a different kinetic model of dynamic strain ageing. Picu (2004) has introduced a new mechanism leading to negative strain-rate sensitivity in dilute solid solutions.

7.2 An Elastic-Viscoplastic Model with "Negative Strain-Rate Sensitivity" of McCormick Type

We consider in the following a phenomenological three dimensional elastic-viscoplastic constitutive model, of "overstress" type, that accounts for negative strain-rate sensitivity. The model formulation is motivated by McCormick's ideas presented in the previous section.

For simplicity reasons the formulation of the problem and its analysis is limited here to small strains and isotropic materials. We denote by $\boldsymbol{\varepsilon}$ the small strain tensor and by $\boldsymbol{\sigma}$ the stress tensor, and by

$$\boldsymbol{e} = \boldsymbol{\varepsilon} - \frac{1}{3}\mathrm{tr}(\boldsymbol{\varepsilon})\boldsymbol{I} \quad \text{and} \quad \boldsymbol{s} = \boldsymbol{\sigma} - \frac{1}{3}\mathrm{tr}(\boldsymbol{\sigma})\boldsymbol{I}, \tag{7.10}$$

their deviatoric parts, respectively. $\boldsymbol{I}$ is the second-order identity tensor.

We consider the additive decomposition of the strain tensor $\boldsymbol{\varepsilon}$ into an elastic and inelastic part, i.e.

$$\boldsymbol{\varepsilon} = \boldsymbol{\varepsilon}^{el} + \boldsymbol{\varepsilon}^{in}. \tag{7.11}$$

with the classical assumption of purely isochoric inelasticity of metals, i.e. $\mathrm{tr}(\boldsymbol{\varepsilon}^{in}) = 0$, it follows that the inelastic strain tensor is a deviatoric one and $\boldsymbol{\varepsilon}^{in} = \boldsymbol{e}^{in}$.

One assumes that the volume deforms only elastically, i.e. the mean strain and the mean stress satisfies the linear relation

$$\mathrm{tr}(\boldsymbol{\sigma}) = 3K\,\mathrm{tr}(\boldsymbol{\varepsilon}), \tag{7.12}$$

where K is the bulk modulus. By assuming that in the elastic domain we have an isotropic Hookean elastic material response, the relation between the stress deviator and the deviatoric part of the elastic strain read as

$$\boldsymbol{s} = 2\mu\boldsymbol{e}^{el}, \tag{7.13}$$

where μ is the shear modulus.

Therefore, the stress tensor can be written as

$$\boldsymbol{\sigma} = \boldsymbol{s} + \frac{1}{3}\mathrm{tr}(\boldsymbol{\sigma})\boldsymbol{I} = 2\mu\boldsymbol{e}^{el} + K\,\mathrm{tr}(\boldsymbol{\varepsilon})\boldsymbol{I} = 2\mu\boldsymbol{\varepsilon}^{el} + \lambda\,\mathrm{tr}(\boldsymbol{\varepsilon}^{el})\boldsymbol{I}, \tag{7.14}$$

where μ and λ are the Lamé coefficients and $K = (2\mu + 3\lambda)/3$.

The inelastic strain tensor is expressed in the fairly general form of the Lévy-von Mises type equation by which its rate is proportional with the deviatoric part of the stress tensor as

$$\dot{\boldsymbol{\varepsilon}}^{in} = \frac{3}{2}\frac{\dot{\varepsilon}^p}{\sigma_{eq}}\boldsymbol{s}, \tag{7.15}$$

where

$$\sigma_{eq} \equiv \sqrt{\frac{3}{2}\boldsymbol{s}\cdot\boldsymbol{s}}, \tag{7.16}$$

and

$$\dot{\varepsilon}^p \equiv \sqrt{\frac{2}{3}\dot{\boldsymbol{\varepsilon}}^{in}\cdot\dot{\boldsymbol{\varepsilon}}^{in}}. \tag{7.17}$$

denote *the equivalent von Mises stress* and *the equivalent inelastic strain-rate*. Here and in the following the over-dot denotes the derivative with respect to time t.

The use of the von Mises equivalent quantities implies plastic isotropy of the material. The specificity of the constitutive model is introduced through a particular form of a kinetic equation relating the equivalent stress σ_{eq} and the equivalent inelastic strain-rate $\dot{\varepsilon}^p$. To describe the PLC effect we choose here as a flow rule a power law of type (7.5), i.e.

$$\dot{\varepsilon}^p = \dot{\varepsilon}_0 \left\langle \frac{\sigma_{eq} - Y(\varepsilon^p, t_a)}{\sigma_D} \right\rangle^m, \tag{7.18}$$

The angle brackets $< \cdot >$ means as usual $< x > = \max(0, x)$ and allow to characterize both the elastic and viscoplastic domains and the loading/unloading conditions. The quantities $\dot{\varepsilon}_0$, m and σ_D are material parameters influencing the kinetics of the viscoplastic processes. The factor $\dot{\varepsilon}_0$, which is proportional to the density of mobile dislocations, is considered constant, $m > 0$ is a constant rate sensitivity parameter and σ_D is a characteristic stress for a dimensionless quantity inside the bracket.

The function $Y = Y(\varepsilon^p, t_a)$ represents the *flow stress*, which depends on the *accumulated plastic strain* ε^p defined as,

$$\varepsilon^p = \int_0^t \sqrt{\frac{2}{3}\dot{\boldsymbol{\varepsilon}}^{in}\cdot\dot{\boldsymbol{\varepsilon}}^{in}}\,\mathrm{d}\tilde{t}, \tag{7.19}$$

and on an internal variable t_a, called *dynamic ageing time*. It is obvious that the rate of the accumulated plastic strain coincides with the equivalent inelastic strain-rate.

The accumulated plastic strain satisfies $\varepsilon^p(0) = 0$, i.e. the body is initially in a virgin state and $\varepsilon^p(t) \geq 0$ increases with time in any elastic-viscoplastic process. One can view ε^p as a macroscopic measure of dislocations stored in the microscopic structure.

Since the expression $\sigma_{eq} - Y(\varepsilon^p, t_a)$ is called *overstress* function, as it characterizes the deviation of the equivalent stress with respect to the flow stress, one says that this elastic-viscoplastic constitutive approach is of *overstress type*. It is obvious, according to (7.18), that the temporal changes in the accumulated plastic strain ε^p are due to the variation of the overstress function and are associated with dissipative effects.

By combining relations (7.11), (7.13), (7.15) and (7.18) one can write the constitutive rate-type equation in terms of the rate of the deviatoric parts of total strain tensor and stress tensor as

$$\dot{\boldsymbol{e}} = \frac{\dot{\boldsymbol{s}}}{2\mu} + \frac{3}{2}\frac{\dot{\varepsilon}_0}{\sigma_{eq}}\left\langle \frac{\sigma_{eq} - Y(\varepsilon^p, t_a)}{\sigma_D} \right\rangle^m \boldsymbol{s}. \tag{7.20}$$

From this expression one can see that we have obtained an elastic-viscoplastic rate-type model with *linear instantaneous response* between the total strain deviator $\boldsymbol{e}$ and the stress deviator $\boldsymbol{s}$. For this class of constitutive relations see also Cristescu and Suliciu (1982, Chap. VIII).

We assume that the flow stress can be decomposed in two additive parts

$$Y(\varepsilon^p, t_a) = \sigma_H(\varepsilon^p) + \sigma_B(\varepsilon^p, t_a), \tag{7.21}$$

where the first term $\sigma_H(\varepsilon^p)$ describes the hardening of the material and the second one $\sigma_B(\varepsilon^p, t_a)$ takes the dynamic strain ageing into account.

One can assume for $\sigma_H(\varepsilon^p)$ a strain dependence obeying a Voce-type equation (see Ling et al. 1993; Böhlke et al. 2009) as

$$\sigma_H(\varepsilon^p) = \sigma_0 + (\sigma_\infty - \sigma_0)\left(1 - \exp\left(-\left(\frac{\Theta_0 \varepsilon^p}{\sigma_\infty - \sigma_0}\right)\right)\right), \tag{7.22}$$

where σ_0 and σ_∞ denote the initial and the saturation values of the stress and Θ_0 is a hardening parameter.

Motivated by relations (7.3) and (7.4), based on the generalization made by Louat (1981) of the relation proposed by Cottrell and Bilby (1949) for the time variation of the solute concentration around dislocations, one can take, according to Böhlke et al. (2009), the part of the stress accounting for the PLC effect as

$$\sigma_B(\varepsilon^p, t_a) = (\sigma_1 + \sigma_2 \varepsilon^p)\left(1 - \exp\left(-\left(\frac{t_a}{t_D}\right)^n\right)\right), \tag{7.23}$$

where t_D is the characteristic time for solute diffusion across dislocations and $n > 0$ is a material parameter.

Let us note that, if one takes the ageing time t_a equal to the waiting time of dislocations t_w, then according to (7.6), one can write relation (7.23) as

$$\sigma_B(\varepsilon^p, t_w) = (\sigma_1 + \sigma_2 \varepsilon^p)\left(1 - \exp\left(-\left(\frac{\Omega(\varepsilon^p)}{t_D \dot{\varepsilon}^p}\right)^n\right)\right). \tag{7.24}$$

It is obvious that when the rate of the accumulated plastic strain $\dot{\varepsilon}^p$ increases, then the waiting time t_w decreases and the stress σ_B also decreases, pointing out in this way a negative strain-rate sensitivity of the flow stress.

Taking into account the relaxation law (7.9), introduced by McCormick (1988), and by using a linear relation of type (7.7) one obtains the following form of the evolution equation for the dynamic ageing time t_a

$$\dot{t}_a = -\frac{\dot{\varepsilon}^p}{\omega_1 + \omega_2 \varepsilon^p} t_a + 1, \tag{7.25}$$

where $\dot{\varepsilon}^p$ is the equivalent inelastic strain-rate (7.18), ε^p is the accumulated plastic strain (7.19) and ω_1 and ω_2 are constant material parameters.

By using expression (7.18), relation (7.25) can be written as

$$\dot{t}_a = -\frac{\dot{\varepsilon}_0}{\omega_1 + \omega_2 \varepsilon^p}\left\langle \frac{\sigma_{eq} - Y(\varepsilon^p, t_a)}{\sigma_D} \right\rangle^m t_a + 1. \tag{7.26}$$

Therefore, the constitutive relations relating the unknowns quantities: the stress $\boldsymbol{\sigma}$, the strain $\boldsymbol{\varepsilon}$, and the internal variable t_a are given by the evolution Eqs. (7.20) and (7.26) completed with relations (7.11–7.17) and (7.19).

These constitutive relations have to be supplemented with the balance of momentum law

$$\rho \frac{\partial \boldsymbol{v}}{\partial t} = \mathrm{div}\boldsymbol{\sigma}, \quad \rho \frac{\partial v_i}{\partial t} = \frac{\partial \sigma_{ij}}{\partial x_j} \tag{7.27}$$

where ρ is the mass density of the material and $\boldsymbol{v} = \boldsymbol{v}(x, t)$ denotes the velocity field and div is the divergence operator with respect to the actual coordinates, written in a Cartesian system in relation $(7.27)_2$.

Let us note that, although the PLC effect manifests only in almost static tests ranging, in general, between 10^{-6} s^{-1} and 10^{-2} s^{-1}, the inertial term in the balance of momentum (7.27) must not be neglected in order to capture the phenomena of strain nucleation and strain localization which accompany the PLC effect as local dynamic events.

7.3 One-Dimensional Stress State

Let us consider a thin bar with uniform cross-section and length L in an undeformed and free-stress state. In studying uniaxial load, or straining, of the bar it is common to make a one-dimensional approximation in which the only non-vanishing stress component is the longitudinal one which is assumed to be uniform in a cross-section. That means, the stress tensor and its deviator in a Cartesian system of coordinate having one of its axes directed along the bar read as

$$\boldsymbol{\sigma} = \begin{pmatrix} \sigma_{11} & 0 & 0 \\ 0 & 0 & 0 \\ 0 & 0 & 0 \end{pmatrix}, \quad \boldsymbol{s} = \begin{pmatrix} \frac{2}{3}\sigma_{11} & 0 & 0 \\ 0 & -\frac{1}{3}\sigma_{11} & 0 \\ 0 & 0 & -\frac{1}{3}\sigma_{11} \end{pmatrix}, \tag{7.28}$$

and the strain tensor and its deviator as

$$\boldsymbol{\varepsilon} = \begin{pmatrix} \varepsilon_{11} & 0 & 0 \\ 0 & \varepsilon_{22} & 0 \\ 0 & 0 & \varepsilon_{22} \end{pmatrix}, \quad \boldsymbol{e} = \begin{pmatrix} \frac{2}{3}(\varepsilon_{11} - \varepsilon_{22}) & 0 & 0 \\ 0 & -\frac{1}{3}(\varepsilon_{11} - \varepsilon_{22}) & 0 \\ 0 & 0 & -\frac{1}{3}(\varepsilon_{11} - \varepsilon_{22}) \end{pmatrix}. \tag{7.29}$$

One assumes also that all the mechanical quantities intervening in the constitutive description depends only on time t and on the spatial variable X corresponding to the axis of the bar.

7.3.1 Constitutive Relations

In this case we denote for simplicity $\sigma = \sigma_{11}$ and $\varepsilon = \varepsilon_{11}$. The elastic deformation of volume (7.11) allows to determine the transversal strain as

$$\varepsilon_{22} = -\frac{\varepsilon}{2} + \frac{\sigma}{6K}. \tag{7.30}$$

Relations (7.11)–(7.13) describing the linear elastic response of the material lead to

$$\varepsilon_{11}^{el} = \frac{(\lambda+\mu)\sigma}{\mu(2\mu+3\lambda)} = \frac{\sigma}{E}, \quad \varepsilon_{22}^{el} = -\frac{\lambda}{2\mu(2\mu+3\lambda)}\sigma, \tag{7.31}$$

where $E = \frac{\mu(3\lambda+2\mu)}{\lambda+\mu}$ is the Young modulus.

By using the additive decomposition of the strain tensor in its elastic and inelastic part, and the fact that the inelastic part is a deviatoric tensor one gets

$$\varepsilon_{11}^{in} = \varepsilon - \frac{\sigma}{E}, \quad \text{and} \quad \varepsilon_{22}^{in} = -\frac{1}{2}\varepsilon_{11}^{in}. \tag{7.32}$$

The equivalent von Mises stress (7.16), the equivalent inelastic strain-rate (7.17) and relation (7.15) read as

$$\sigma_{eq} = |\sigma|, \quad \dot{\varepsilon}^p = \left|\dot{\varepsilon}_{11}^{in}\right| = \left|\dot{\varepsilon} - \frac{\dot{\sigma}}{E}\right|, \quad \dot{\varepsilon} - \frac{\dot{\sigma}}{E} = \frac{\sigma}{|\sigma|}\left|\dot{\varepsilon} - \frac{\dot{\sigma}}{E}\right|. \tag{7.33}$$

The accumulated plastic strain (7.19) becomes

$$\varepsilon^p(t) = \int_0^t \left|\dot{\varepsilon}_{11}^{in}(s)\right| \mathrm{d}s = \int_0^t \left|\dot{\varepsilon}(s) - \frac{\dot{\sigma}(s)}{E}\right| \mathrm{d}s \geq 0. \tag{7.34}$$

Then, the tensorial viscoplastic constitutive relation (7.20) reduces to a single equation

$$\dot{\varepsilon} = \frac{\dot{\sigma}}{E} + \dot{\varepsilon}_0 \left\langle \frac{|\sigma| - Y(\varepsilon^p, t_a)}{\sigma_D} \right\rangle^m \frac{\sigma}{|\sigma|}. \tag{7.35}$$

Let us consider the case of a *tensile* test, that is $\sigma > 0$. Then, according to $(7.33)_3$, $|\dot{\varepsilon} - \dot{\sigma}/E| = \dot{\varepsilon} - \dot{\sigma}/E > 0$, and the accumulated plastic strain (7.34) becomes $\varepsilon^p(t) = \varepsilon(t) - \sigma(t)/E$, if the bar at the initial moment is undeformed, i.e. $\varepsilon(0) - \sigma(0)/E = 0$. Then, the constitutive Eq. (7.35) can be written as

$$\dot{\sigma} = E\dot{\varepsilon} - E\dot{\varepsilon}_0 \left\langle \frac{\sigma - Y\left(\varepsilon - \frac{\sigma}{E}, t_a\right)}{\sigma_D} \right\rangle^m. \tag{7.36}$$

For the *compressive* case, that is when $\sigma < 0$, according to $(7.33)_3$, we have $|\dot{\varepsilon} - \dot{\sigma}/E| = -\dot{\varepsilon} + \dot{\sigma}/E > 0$, and the accumulated plastic strain (7.34) is $\varepsilon^p(t) = -\varepsilon(t) + \sigma(t)/E$, if the bar at the initial moment is undeformed, i.e. $\varepsilon(0) - \sigma(0)/E = 0$. Then, the constitutive Eq. (7.35) can be written as

$$\dot{\sigma} = E\dot{\varepsilon} - E\dot{\varepsilon}_0 \left\langle \frac{-\sigma - Y\left(-\varepsilon + \frac{\sigma}{E}, t_a\right)}{\sigma_D} \right\rangle^m. \tag{7.37}$$

By combining relations (7.36) and (7.37) we can write the constitutive Eq. (7.35) in the form

$$\frac{\partial \sigma}{\partial t} - E\frac{\partial \varepsilon}{\partial t} = G(\varepsilon, \sigma, t_a), \tag{7.38}$$

where

$$G(\varepsilon,\sigma,t_a)=-\frac{E\dot{\varepsilon}_0}{\sigma_D^m}\begin{cases}\left(\sigma-Y\left(\varepsilon-\frac{\sigma}{E},t_a\right)\right)^m, & \text{if } \sigma>Y\left(\varepsilon-\frac{\sigma}{E},t_a\right)\\ 0, & \text{if } -Y\left(-\varepsilon+\frac{\sigma}{E},t_a\right)\le\sigma\le Y\left(\varepsilon-\frac{\sigma}{E},t_a\right)\\ \left(-\sigma-Y\left(-\varepsilon+\frac{\sigma}{E},t_a\right)\right)^m, & \text{if } \sigma<-Y\left(-\varepsilon+\frac{\sigma}{E},t_a\right).\end{cases}$$

The evolution equation for the dynamic ageing time (7.25) can then be written as

$$\frac{\partial t_a}{\partial t}=H(\varepsilon,\sigma,t_a), \tag{7.39}$$

where

$$H(\varepsilon,\sigma,t_a)=\begin{cases}\frac{G(\varepsilon,\sigma,t_a)}{E\left(\omega_1+\omega_2\left(\varepsilon-\frac{\sigma}{E}\right)\right)}t_a+1, & \text{if } \sigma>Y\left(\varepsilon-\frac{\sigma}{E},t_a\right)\\ 1, & \text{if } -Y\left(-\varepsilon+\frac{\sigma}{E},t_a\right)\le\sigma\le Y\left(\varepsilon-\frac{\sigma}{E},t_a\right)\\ \frac{G(\varepsilon,\sigma,t_a)}{E\left(\omega_1+\omega_2\left(-\varepsilon+\frac{\sigma}{E}\right)\right)}t_a+1, & \text{if } \sigma<-Y\left(-\varepsilon+\frac{\sigma}{E},t_a\right).\end{cases}$$

Here function $Y=Y(\varepsilon^p,t_a)$ is given by relations (7.21)–(7.23).

7.3.2 *Field Equations and Initial-Boundary Value Problems*

To investigate the predictions of the model we have to consider besides the constitutive relations (7.38) and (7.39) the partial differential equations governing the longitudinal motion of a thin bar with constant mass density ρ in the reference configuration. These are the balance of momentum and the compatibility equation between strain and velocity

$$\rho\frac{\partial v}{\partial t}-\frac{\partial\sigma}{\partial X}=0,\quad \frac{\partial\varepsilon}{\partial t}-\frac{\partial v}{\partial X}=0, \tag{7.40}$$

where t is time, $X\in[0,L]$ is the (Lagrangian) spatial coordinate along the bar and v is the particle velocity. Once more, the inertial term is not neglected in order to be able to capture the local dynamic events.

Hence, the complete PDEs system in the unknown $\sigma=\sigma(X,t)$, $\varepsilon=\varepsilon(X,t)$, $t_a=t_a(X,t)$ and $v=v(X,t)$ composed by the Eqs. (7.38), (7.39) and (7.40) can be written as

$$\frac{\partial}{\partial t}\begin{pmatrix}v\\ \varepsilon\\ \sigma\\ t_a\end{pmatrix}+\begin{pmatrix}0 & 0 & -1/\rho & 0\\ 1 & 0 & 0 & 0\\ -E & 0 & 0 & 0\\ 0 & 0 & 0 & 0\end{pmatrix}\frac{\partial}{\partial X}\begin{pmatrix}v\\ \varepsilon\\ \sigma\\ t_a\end{pmatrix}=\begin{pmatrix}0\\ 0\\ G(\varepsilon,\sigma,t_a)\\ H(\varepsilon,\sigma,t_a)\end{pmatrix}. \tag{7.41}$$

The type of the system is given by its characteristic directions $\mathrm{d}X/\mathrm{d}t = r$ which are defined as the eigenvalues of the 4×4 matrix in (7.41). These are $(\mathrm{d}X/\mathrm{d}t)^2 = E/\rho > 0$ and $(\mathrm{d}X/\mathrm{d}t)^2 = 0$. They are real and positive and consequently the system is *hyperbolic*. Moreover, it is *semilinear with source terms* since all the nonlinear terms, i.e. G and H, are among the free terms of the system.

As we have seen in Sect. 7.1.1 the PLC phenomenon is usually investigated by two kind of experiments: either a tensile testing at constant applied strain-rate ("hard testing machine experiment"), or a tensile testing at constant applied stress-rate ("soft testing machine experiment").

To simulate such kind of uniaxial quasi-static experiments we have to consider a bar initially at rest, in its natural state of strain and stress, with one of its end fixed. The other end is subjected to one of the following conditions.

(*A*) *Strain–controlled experiment – cross-head velocity controlled experiment.*
The left-end of the bar in this tensile test is moved with a constant negative velocity V^*. Thus, we have to find the solution of the system (7.41) which satisfies the initial and boundary conditions.

$$\begin{aligned} &\varepsilon(X,0) = 0, \quad \sigma(X,0) = 0, \quad t_a(X,0) = 0, \quad v(X,0) = 0, \quad \text{for } X \in [0,L], \\ &v(0,t) = V^*, \quad v(L,t) = 0 \quad \text{for any } t > 0. \end{aligned} \tag{7.42}$$

This experiment corresponds to an engineering constant strain-rate $\dot{\varepsilon}_e = |V^*|/L$.

(*B*) *Stress–controlled experiment – true constant stress-rate experiment.*
The end of the bar is submitted to a constant increase of the load. Thus, we have to find the solution of the system (7.41) which satisfies the initial and boundary conditions.

$$\begin{aligned} &\varepsilon(X,0) = 0, \quad \sigma(X,0) = 0, \quad t_a(X,0) = 0, \quad v(X,0) = 0, \quad \text{for } X \in [0,L], \\ &\sigma(0,t) = \dot{\sigma}_e t, \quad v(L,t) = 0 \quad \text{for any } t > 0, \end{aligned} \tag{7.43}$$

where the applied stress-rate $\dot{\sigma}_e = \text{const.} > 0$.

(*C*) *Mixed stress- and strain-controlled experiment – pseudoconstant stress-rate experiment.*
As we have seen in the comments from Sect. 7.1.1 related with Figs. 7.4 and 7.5 a true constant stress-rate test is very difficult to be conducted in laboratory experiments by conventional testing machines due to the elastic interaction between specimen and the testing machine which is caused by the spring introduced between the specimen and the grips of the machine. In order to take into account the influence of the testing machine we consider that in fact the left-end condition is a mixture between a perfect hard testing-machine and a pure soft-testing machine by considering the following mixed initial-boundary value problem.

$$\varepsilon(X,0)=0,\quad \sigma(X,0)=0,\quad t_a(X,0)=0,\quad v(X,0)=0,\quad \text{for } X\in[0,L],$$
$$\beta\sigma(0,t)-(1-\beta)\sqrt{\rho E}v(0,t)=\beta\dot{\sigma}_e t-(1-\beta)\sqrt{\rho E}V^*, v(L,t)=0 \text{ for any } t>0, \tag{7.44}$$

where $\dot{\sigma}_e = \text{const.} > 0$, $V^* = \text{const.} < 0$ and β is a parameter with the property that $\beta \in [0,1]$.

It is obvious that when $\beta = 1$ we simulate a constant stress-rate test, while when $\beta = 0$ we simulate a constant strain-rate test ($\dot{\varepsilon}_e = V^*/L$). For $\beta \in (0,1)$ we have a mixed boundary condition. If β is near 1, this boundary condition should correspond to a "pseudoconstant" stress-rate experiment.

To solve these initial–boundary value problems for the system of PDEs (7.41), and see what the model predicts, we built an explicit second order finite difference numerical scheme based on the method of characteristics. This is described in Appendix.

7.3.3 A Numerical Investigation

The mechanical parameters of the model are listed in the fifth column of Tables 7.1 and 7.2 and are chosen in agreement with similar parameters in the literature, but so as to ensure the fulfillment of critical conditions for the emergence of typical instability phenomena for the PLC effect. These conditions are investigated in Sect. 7.4.

We consider here a bar of length $L = 20$ mm discretized by using 161 nodes, that means a space integration step $h = 0.125$ mm and a time integration step $\tau = 3.44 \times 10^{-8}$ s satisfying condition (7.71) for the Courant number $\nu = 0.9$. Since the numerical experiments simulate laboratory tests at extremely low strain-rates an important computation time was necessary.

Table 7.1 Mechanical parameters for classical part of elastic-viscoplastic relations (7.20)–(7.22)

Parameters	Zhang et al. (2001)	Benallal et al. (2008a, b), Zhang et al. (2012)	Böhlke et al. (2009)	This paper	Units
E	70	70	70	70	GPa
ρ	–	–	–	6550	kg/m^3
$\dot{\varepsilon}_0$	2.3×10^{-7}	10^{-8}	3.5×10^{-5}	3.5×10^{-6}	s^{-1}
σ_D	(0.41, 1.7)	2.23	15.	30	MPa
m	Exponential (7.3)	Exponential (7.3)	28	15	
σ_0	38.3	78.7	123	123	MPa
σ_∞	67.9	Power law	343	343	MPa
Θ_0	534.6		2800	2800	MPa

Table 7.2 Mechanical parameters for the DSA model described by (7.26) and (7.23)

Parameters	Zhang et al. (2001)	Benallal et al. (2008a, b), Zhang et al. (2012)	Böhlke et al. (2009)	This paper	Units
σ_1	$(7.92, 30.6)$	62.22	18.9	62.22	MPa
σ_2	–	0	189.26	622.2	MPa
t_D	$(0.126, 0.03)$	0.02	0.125	0.125	s
n	$1/3$	$1/3$	1/3	1/3	
ω_1	$(3.6 \times 10^{-5}, 7.9 \times 10^{-4})$	10^{-4}	6.81×10^{-4}	3.6×10^{-5}	
ω_2	–	0	3.6×10^{-4}	0	
$A = \frac{n\sigma_1}{\omega_1 E}$	$(0.23, 1.05)$	$2.96 > e$	$0.132 < e$	$8.23 > e$	
Temporal instability	No	Yes	No	Yes	

The numerical results show that the constitutive model is able to reproduce with reasonable accuracy most of the experimentally observed phenomena which accompany the PLC effect.

7.3.3.1 Strain-Controlled Experiments

We first consider the constant strain-rate experiment (7.42) where the free-end of the bar is moved with the constant velocity $V^* = 0.2$ mm/s, which corresponds to the engineering strain-rate $\dot{\varepsilon}_e = 10^{-3}\text{s}^{-1}$.

The computed stress–engineering strain curve, i.e. the end-stress $\sigma(0,t)$ versus $\varepsilon_e(t) = \frac{1}{L}\int_0^L \varepsilon(X,t)\text{d}X = (l(t) - L)/L$, where $l(t)$ is the actual length of the bar, is illustrated in Fig. 7.6. One obtains a serrated curve, with sudden stress drops ("jerky flow") and with a changes of the serrated plateaus. The emergence of different serrated yielding plateaus in a constant strain-rate experiment is often reported in laboratory tests on alloys which present the PLC effect as it is shown in Fig. 7.7. No geometric defect, or other heterogeneity was introduced in the PDEs system to initiate the unstable behavior of the solution.

The same as in the laboratory experiments, the serrations accompany the formation of bands of localized deformation in the bar. Indeed, the numerical experiment clearly illustrates how the strain bands nucleate, localize and propagate along the specimen. For instance, if one focuses on the zoom in Fig. 7.6 one can follow in Fig. 7.8 the evolution of the strain and strain-rate distribution in bar during the stress oscillations. Thus, between the points A and B the stress rises elastically and when it reaches a critical value it suddenly drops. During this slowly and almost elastic process the strain band distribution in the bar remains unchanged and there is

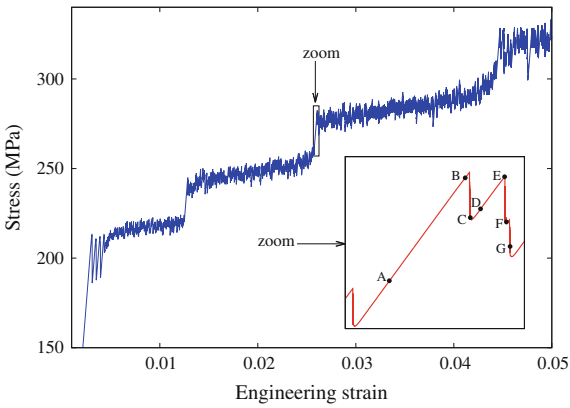

Fig. 7.6 Serrated stress-strain curve for numerical simulation of a hard-testing machine experiment with engineering strain-rate $\dot{\varepsilon}_e = 10^{-3}\ s^{-1}$. Insert: zoom of a portion and the position of points A, B, C, D, E, F, G where are recorded the distribution of strain ε and strain-rate $\dot{\varepsilon}$ in bar, illustrated in Fig. 7.8

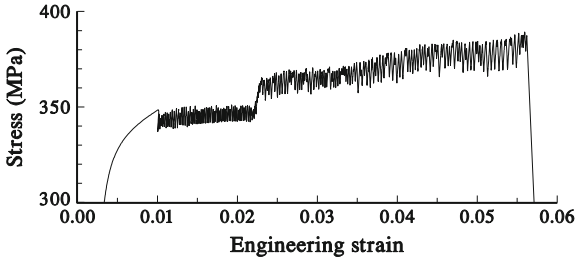

Fig. 7.7 Nominal stress versus engineering strain in constant strain-rate test at $\dot{\varepsilon}_e = 10^{-5}\ s^{-1}$ in 5182H28 alloy. Serrated flow with change of plateaus (reproduced with permission from Făciu et al. (1998) EDP Sciences)

no significant plastic activity. Only at point B, just before the stress drop, the plastic activity begins to activate and the strain-rate in the bar locally overcomes the value of the imposed strain-rate announcing the apparition of a new localization of strain. During the stress drop, at the level of point C, a new strain band appears and inside this band it is observed that the strain-rate is six hundred times larger than the applied strain-rate. At the end of the stress drop, the new band is already buildup and the plastic activity goes out at the point D.

Once the stress starts to rise again elastically, between the points D and E, the strain band distribution remains unchanged and the process is quasistatic (compare the strain and the strain-rate distribution at the points C, D and E in Fig. 7.8). Only at point E, just before a new stress drop, the strain-rate starts to increase locally marking the new nucleation zones. Two new dynamic events follow. A stress drop to the point F, which leads to the localization of the strain near the fixed end of the bar, followed immediately by a sudden stress decay at the point G which leads to the apparition of a new localization of strain. These two strain bursts are accompanied by an important increase of the strain-rate inside the new bands, which becomes at the point G more than four thousand times higher than the imposed strain-rate. This behavior is in agreement with the laboratory experiment illustrated in Fig. 7.3. The process continues in this way in a manner almost cyclic.

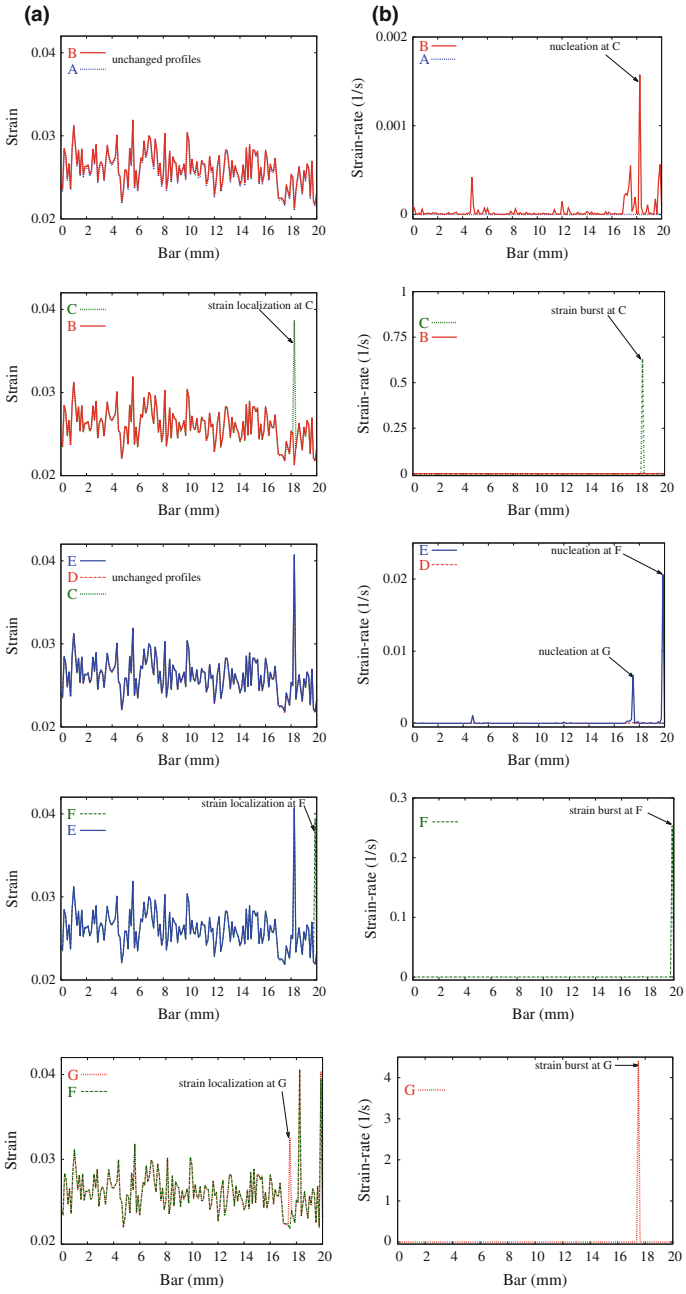

Fig. 7.8 **a** The distribution of strain ε and **b** The distribution of strain-rate $\dot{\varepsilon}$ in bar at the moments A, B, C, D, E, F, G in Fig. 7.6. Note the different scales used for the strain-rate distribution

It is obvious that the stress drop occurs in a time interval much smaller than that required for the new increase of the stress. Therefore, the sawtooth appearance of the stress-strain curve reflects an alternation between dynamic and quasi-static processes. Thus, Fig. 7.8 also illustrates how the stress drop is accompanied by local dynamic events followed by quasi-static ones. This behavior explains the mechanism of "go-and-stop" propagation of strain bands which is recorded in laboratory experiments.

An overview of the PLC band propagation in the numerical simulation in Fig. 7.6 is illustrated in Fig. 7.9. One can see that the strain bands nucleate in a way specifically to the type B bands, which appear as hopping bands propagating discontinuously, in an intermittent manner.

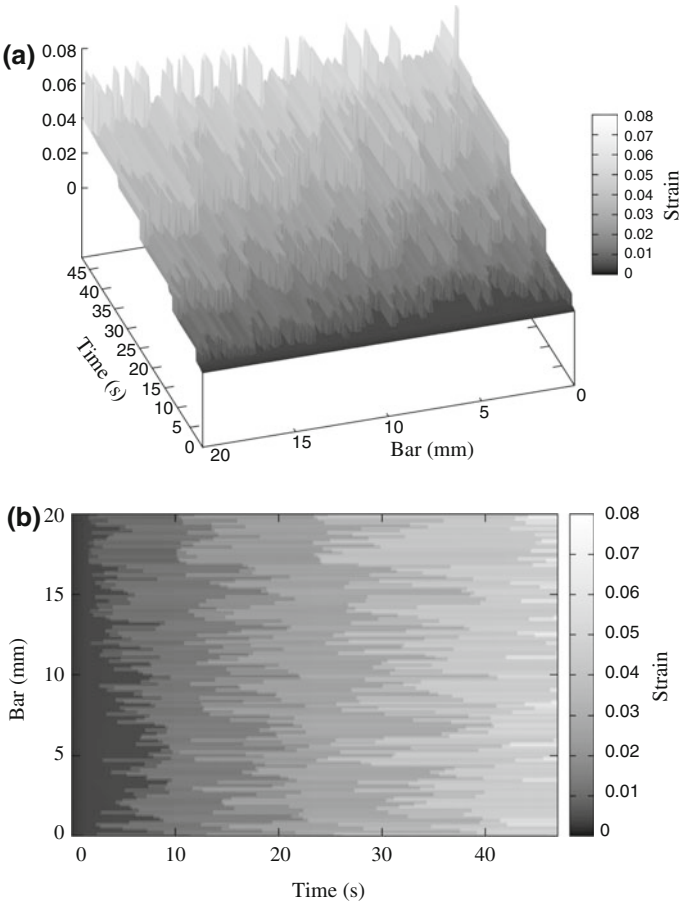

Fig. 7.9 Overall picture of the strain evolution in the bar during the cross-head velocity controlled experiment in Fig. 7.6. **a** Spatial representation of $\varepsilon = \varepsilon(X, t)$. **b** Its plane projection

Let us also note that each plateau of the serrated curve corresponds to a new stage of the strain growth in bar during the plastic deformation. Thus, for the numerical simulation illustrated in Fig. 7.6 there are four plateaus which lead to four stages of strain increase as can be seen in Fig. 7.9.

One observes that the increase of the local strain along a plateau, in general, is not larger than the maximal value of the engineering strain of the corresponding plateau. Indeed, see for instance the size of the strain bursts in Fig. 7.8 and compare with the value of the engineering strain at the end of the corresponding plateau.

Therefore, such numerical simulations could clarify the relation between the strain magnitude of a serrated yielding plateau and the way the strain increases inside a band during a stress drop. Thus, one could explain, depending on the "jerky" flow structure of the serrated curve, the possible occurrence of visible strain markings on the surface of a specimen during its unstable viscoplastic flow.

The 3D Fig. 7.10 illustrates how the plastic strain-rate is locally activated in a spectacular way in the process of band formation during each stress drop. Since these simulations are demanding not only with respect to the computation time, but also to the data storage it is possible to not capture here the largest strain-rates of the numerical simulation.

The evolution of the ageing time variable t_a describes the dynamic ageing process in which dislocations are alternately pinned by solute and released, or newly generated, when the stress attains some critical value.

This behavior is illustrated in Fig. 7.11. According to the evolution Eq. (7.26) when a particle of the bar suffers an elastic quasi-static process one has $\frac{dt_a}{dt} = 1$, that is, one has a linear increase of t_a with constant slope 1. This behavior can be clearly seen appearing regularly in Fig. 7.11. The increase of the ageing time during the slow elastic stress growth describes in fact the process of ageing of dislocations

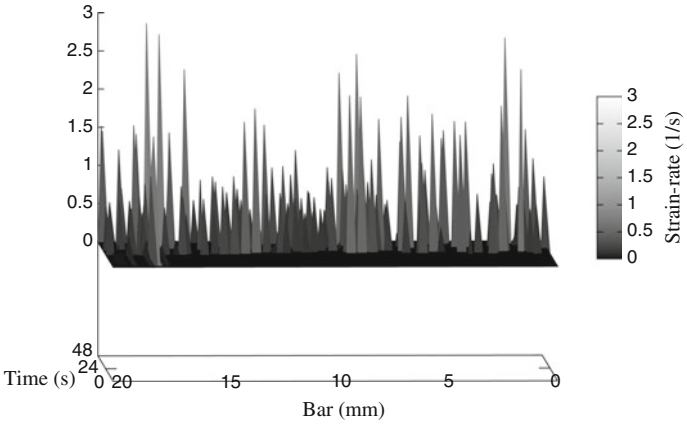

Fig. 7.10 Overall picture of the strain-rate $\dot{\varepsilon} = \dot{\varepsilon}(X, t)$ in the bar during the cross-head velocity controlled experiment in Fig. 7.6

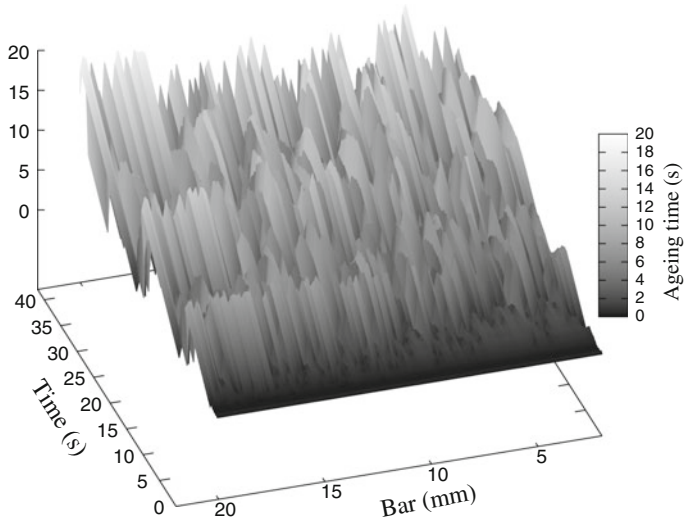

Fig. 7.11 Overall picture of the evolution of the ageing time $t_a = t_a(X, t)$ in the bar during the cross-head velocity controlled experiment in Fig. 7.6

when the band front is pinned. Afterwards, the ageing time of the particles which enter the viscoplastic domain starts to decay.

During the nucleation and localization process, when the stress sharply decreases and the strain-rate bursts leading to localized bands, the ageing time t_a decreases rapidly to the waiting time $t_w \approx \Omega/\dot{\varepsilon}_e = 3.5 \times 10^{-2}$s in the corresponding zones, as can be seen in Fig. 7.12 (compare the ageing time distribution in the bar at points B and C). This behavior is in agreement with Schwarz (1985) assertion that the propagation and localization occur at the position of less aged dislocations. This can

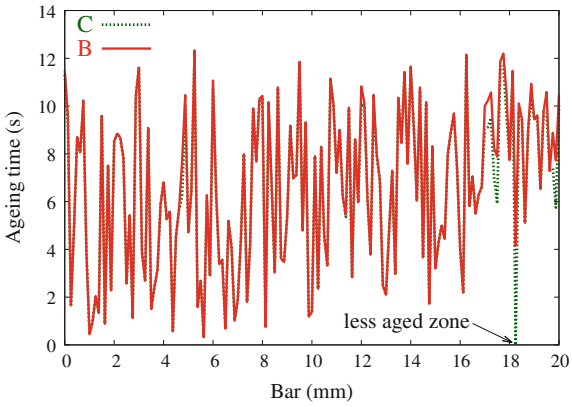

Fig. 7.12 The distribution of the ageing time t_a in bar during a stress drop—moments B and C in Fig. 7.6

be also observed globally in Fig. 7.11 where t_a decreases for short periods of time in the neighborhood of the new localized front bands.

Thus, the prediction of the model is in agreement with the observation made by Cuddy and Leslie (1972) that, as the bands appear along the gauge length, producing regular serrations on the load-extension curve, and surface markings on the specimen, there is an alternation between the ageing and breakaway of the dislocations.

We end the comments on strain-controlled experiments with Fig. 7.13 which illustrates how the strain-rate influences the yielding curve. One observes that, as the engineering strain-rate $\dot{\varepsilon}_e$ decreases, the stress-strain curves, in general, move up pointing out the way the constitutive equations describe the negative strain-rate sensitivity of the flow stress. For $\dot{\varepsilon}_e = 10^{-1}\text{s}^{-1}$ there is only a first drop, but no jerky flow appears. The reason is that at this "high" strain-rate we are outside the region of instability predicted by the analytical results in Sect. 7.4 for the material parameters in Tabels 7.1 and 7.2. As we have already seen, the numerical simulation performed at $\dot{\varepsilon}_e = 10^{-3}\text{s}^{-1}$ presents the characteristics of type B serrations and PLC bands propagation, with regular alternation of stress increases and decreases. For the increasing engineering strain-rate $\dot{\varepsilon}_e = 10^{-2}\text{s}^{-1}$, which according to the stability analysis in the next section, lies in the intermediate range of stable/unstable flow, the stress-strain curve presents the characteristics of a transition from type A to type B serrations with more irregular humps and valleys.

The stress drop amplitudes also show a slight strain dependence, in agreement with laboratory experiments, which points out a gradual increase of the serrations with strain (see Fig. 7.1). Thus, the overall agreement of the numerical simulations with experiments is found to be reasonable.

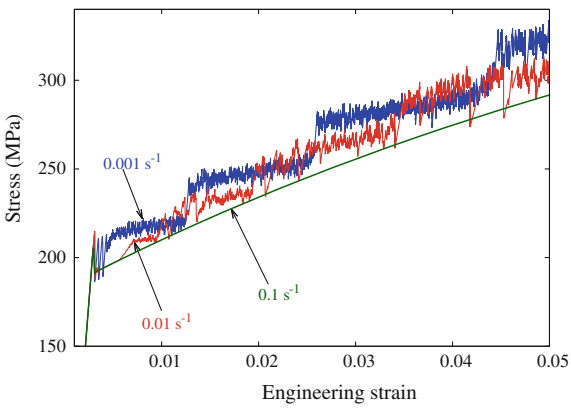

Fig. 7.13 Influence of the imposed engineering strain-rate $\dot{\varepsilon}_e$ on the serrated yielding

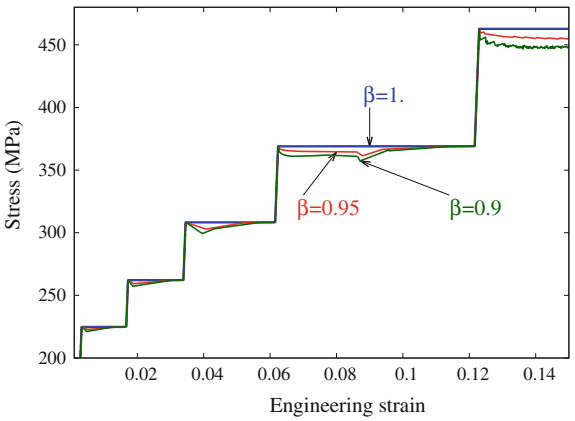

Fig. 7.14 Staircase type stress-strain curves in the numerical simulation of a soft-testing machine experiment. $\beta = 1$ corresponds to a true constant stress-rate test (7.43) at $\dot{\sigma}_e = 10$ MPa/s. $\beta = 0.95$ and $\beta = 0.9$ correspond to the mixed boundary condition (7.44) where $\dot{\sigma}_e = 10$ MPa/s and $V^* = 2.85 \times 10^{-3}$ mm/s ($\dot{\varepsilon}_e = 1.4 \times 10^{-3}$ s^{-1}, i.e. $\dot{\sigma}_e = E\dot{\varepsilon}_e$)

7.3.3.2 Stress-Controlled Experiments

We first consider a numerical simulation of the *true* constant stress-rate test (7.43) (or equivalently, (7.44) for $\beta = 1$) with $\dot{\sigma}_e = 10$ MPa/s. The computed end-stress $\sigma(0,t)$ vs. engineering strain $\varepsilon_e(t)$ illustrates in Fig. 7.14 how the model is able to predict a staircase structure with five steps, each one corresponding to a strain burst.

At the scale of the 3D picture in Fig. 7.15 the specimen appears to deform in a homogeneous manner along the almost horizontal treads, but also on the vertical risers where the sudden strain bursts occurs leading to the increase of deformation by steps. The transition from one strain burst plateau in Fig. 7.14 to the next one is a quasistatic process with practically no plastic activity. The alternation between these quasistatic and dynamic events is illustrated in Fig. 7.16 where it is depicted

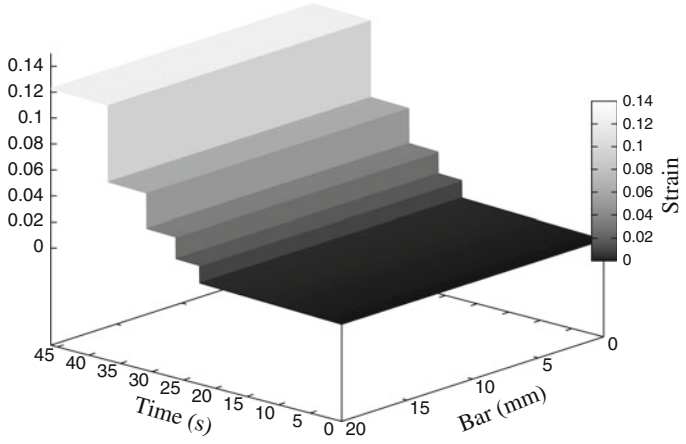

Fig. 7.15 Overall picture of the strain $\varepsilon = \varepsilon(X,t)$ in the bar during the true constant stress-rate experiment ($\beta = 1$) in Fig. 7.14

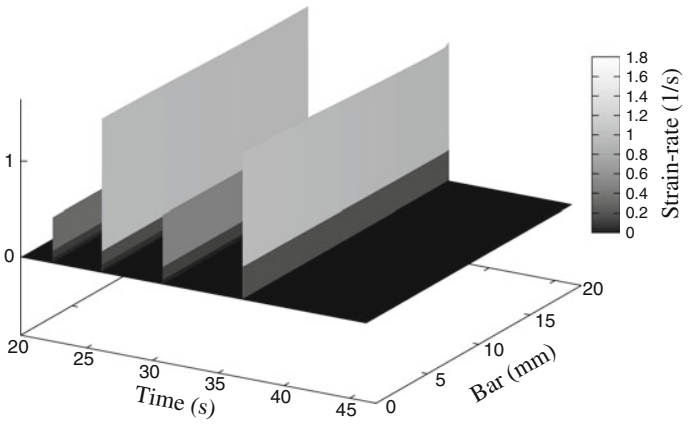

Fig. 7.16 Overall picture of the strain-rate $\dot{\varepsilon} = \dot{\varepsilon}(X,t)$ in the bar during the true constant stress-rate experiment ($\beta = 1$) in Fig. 7.14

the evolution of the strain-rate for the first four plateaus in Fig. 7.14. The prediction of the model for this ideal testing case is in agreement with the remark by Cuddy and Leslie (1972) according to which "in a soft machine where the applied load remains constant, the band spreads immediately over the entire gauge length."

The evolution of the ageing time variable t_a is illustrated in Fig. 7.17. One has a homogeneous and linear increase of the ageing time with constant slope 1 during the quasi-static elastic deformation of the bar. This corresponds to the ageing of dislocations when they are arrested at local obstacles.

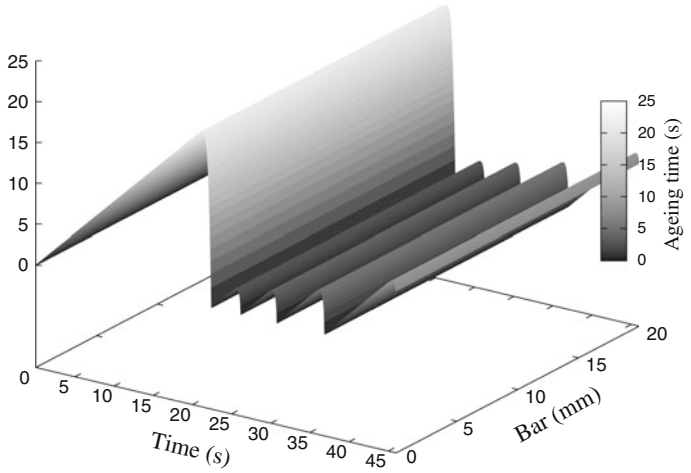

Fig. 7.17 Overall picture of the ageing time $t_a = t_a(X,t)$ in the bar during the true constant stress-rate experiment ($\beta = 1$) in Fig. 7.14

Afterwards, when the stress attains some critical value, a decay of t_a in the viscoplastic domain starts and is followed, during the strain burst, by a sudden drop near zero. This behavior corresponds to the moment when the dislocations become unlocked, start to move, accelerate rapidly and advance to the next obstacles. At the end, when the strain reaches a certain level, the advancing of the deformation front stops and the process is restarted.

As we have seen in the Sect. 7.1.1, the experimental literature points out that macroscopic features of the PLC effect, like the stress-engineering strain curves, depend strongly on the testing machine. In order to examine the sensitivity of the model to a perturbation of the mode of testing we considered the mixed initial-boundary value problem (7.44) to simulate the so called pseudoconstant-$\dot{\sigma}_e$ experiments. The way the model is able to simulate the influence of the machine effects is illustrated in Fig. 7.14 where the computed stress-strain curves obtained for $\beta = 0.95$ and $\beta = 0.9$ are represented. These numerical simulations with mixed boundary conditions are closer to the laboratory experiments of pseudoconstant stress-rate experiments illustrated in Fig. 7.5, or reported in Fellner et al. (1991, Figs. 3–4). Indeed, one gets numerically, the same as in the experiments mentioned earlier that, instead of a horizontal plateau during the strain burst, we firstly have a stress decay followed by an increase to the level of the horizontal plateau. The decrease is more important as the parameter β has a smaller value than 1. Much more than that, one observes, for $\beta = 0.9$ and for large strain, that the decrease of the stress is accompanied by oscillations. This behavior is in agreement with the remark made in Fellner et al. (1991) that *when 'constant-$\dot{\sigma}_e$' tests are carried out on electronically controlled tensile machines, it is not completely possible to avoid an initial stress drop and successive 'oscillations'*. Moreover, for such pseudoconstant-$\dot{\sigma}_e$ simulations like in Fig. 7.14 it is expected that the strain will no longer propagate in a homogeneous manner and some localization phenomena will appear during the strain burst.

7.4 A Methodology for Investigating Mechanical Parameters for Critical Conditions on PLC Effect

The question which arises is how one can identify the range of boundary conditions and the range of mechanical parameters of the model described in Sect. 7.2 for which the main characteristics of the PLC effect occur and how one can fit the numerical simulations with experimental tests.

In this section we give a partial answer to this problem. For instance, in order to determine for which input data, that is, for which mechanical parameters and imposed engineering strain-rate, there exists a jerky flow, we consider a stability analysis of a particular solution of the PDEs system (7.41). This allows the calibration and verification of the constitutive model. A stability and bifurcation analysis for investigating the PLC effect has been also used by Mesarovics (1995), Rizzi and Hähner (2004).

7.4.1 Temporal Stability Analysis of Serrated Curves

We analyze in the following the nature of temporal instabilities and, as a consequence, the existence or non-existence of serrations on the stress–engineering strain curve. For doing this, we consider instead of the strain-controlled problem (7.42) the following related initial-boundary value problem

$$\begin{aligned} &\varepsilon(X,0)=\varepsilon^*,\ \sigma(X,0)=\sigma^*,\ t_a(X,0)=t_a^*,\ v(X,0)=\frac{V^*}{L}(L-X),\ \text{for } X\in[0,L],\\ &v(0,t)=V^*=-L\dot{\varepsilon}_e<0,\quad v(L,t)=0,\quad \text{for any } t>0. \end{aligned} \tag{7.45}$$

That means, at the initial moment the bar is not at rest, but the velocity field is linear with respect to the spatial variable and satisfies the boundary conditions corresponding to a strain-controlled experiment.

In this special case the PDEs system (7.41) admits the following *spatial homogeneous solution* in the variables ε, σ and t_a, i.e.

$$\varepsilon=\varepsilon(t)=-\frac{V^*}{L}t=\dot{\varepsilon}_e t,\quad \sigma=\sigma(t),\quad t_a=t_a(t),\quad v=v(X)=\frac{V^*}{L}(L-X), \tag{7.46}$$

where $\sigma(t)$ and $t_a(t)$ are determined as solution of an ordinary differential equations (ODE) system. Taking into account that between ε and t there is a linear relation we can express the variable σ and t_a as function of ε. Functions $\sigma=\sigma(\varepsilon)$ and $t_a=t_a(\varepsilon)$ have to be solution of the Cauchy problem for the non-linear and *non-autonomous* system

$$\begin{cases} \frac{\mathrm{d}\sigma}{\mathrm{d}\varepsilon}=E+\frac{1}{\dot{\varepsilon}_e}G(\varepsilon,\sigma(\varepsilon),t_a(\varepsilon)), & \sigma(\varepsilon^*)=\sigma^*,\\ \frac{\mathrm{d}t_a}{\mathrm{d}\varepsilon}=\frac{1}{\dot{\varepsilon}_e}H(\varepsilon,\sigma(\varepsilon),t_a(\varepsilon)), & t_a(\varepsilon^*)=t_a^*. \end{cases} \tag{7.47}$$

To simplify the stability analysis of the system (7.47) we consider the case when the constitutive functions σ_H, σ_B in (7.21) and Ω in (7.7) do not depend on ε^p, i.e. when the ODE system is *autonomous*. That means $\sigma_\infty=0$, $\Theta_0=0$, $\sigma_2=0$ and $\omega_2=0$, i.e.

$$\sigma_H(\varepsilon^p)=\sigma_0,\quad \sigma_B(\varepsilon^p,t_a)=\sigma_1\left(1-\exp\left(-\frac{t_a}{t_D}\right)^n\right),\quad \Omega(\varepsilon^p)=\omega_1. \tag{7.48}$$

Thus, the solution of the system (7.47) satisfies the Cauchy problem

$$\begin{cases} \frac{\mathrm{d}\sigma}{\mathrm{d}\varepsilon}=E, & \sigma(\varepsilon^*)=0,\\ \frac{\mathrm{d}t_a}{\mathrm{d}\varepsilon}=\frac{1}{\dot{\varepsilon}_e}, & t_a(\varepsilon^*)=0, \end{cases} \tag{7.49}$$

if it lies in the *elastic domain*, that is, for

$$|\sigma| \leq \sigma_0 + \sigma_1(1 - \exp(-(t_a/t_D)^n),$$

and, it satisfies the Cauchy problem

$$\begin{cases} \frac{\mathrm{d}\sigma}{\mathrm{d}\varepsilon} = & f(\sigma, t_a) \equiv E - E\frac{\dot{\varepsilon}_0}{\dot{\varepsilon}_e}\left[\frac{\sigma-\sigma_0-\sigma_1(1-\exp(-(t_a/t_D)^n)}{\sigma_D}\right]^m, \\ & \sigma(\varepsilon^*) = \sigma^*, \\ \frac{\mathrm{d}t_a}{\mathrm{d}\varepsilon} = & g(\sigma, t_a) \equiv -\frac{\dot{\varepsilon}_0}{\omega_1\dot{\varepsilon}_e}\left[\frac{\sigma-\sigma_0-\sigma_1(1-\exp(-(t_a/t_D)^n)}{\sigma_D}\right]^m t_a + \frac{1}{\dot{\varepsilon}_e}, \\ & t_a(\varepsilon^*) = t_a^*. \end{cases} \tag{7.50}$$

if the solution belongs to the *viscoplastic domain in tension*, that is, for

$$\sigma > \sigma_0 + \sigma_1(1 - \exp(-(t_a/t_D)^n).$$

First, we investigate only the behavior of a homogeneous process in the viscoplastic domain, i.e. the solutions of the non-linear autonomous system (7.50). Thus, we do not consider at this moment the case when the homogeneous solution could enter in the elastic domain and has to satisfy the system (7.49). The combined elastic-viscoplastic homogeneous solution for the non-autonomous system is considered later and illustrated numerically for the mechanical parameters in Tables 7.1 and 7.2 in Fig. 7.24.

To sketch the phase portrait of a dynamical system it is useful to plot the nullclines, defined as the curve where $\frac{\mathrm{d}\sigma}{\mathrm{d}\varepsilon} = 0$ and $\frac{\mathrm{d}t_a}{\mathrm{d}\varepsilon} = 0$. The equilibrium points, or the fixed points of the system are defined as the intersection points of the curves $f(\sigma, t_a) = 0$ and $g(\sigma, t_a) = 0$. The system (7.50) has a unique fixed point

$$t_a^{fx} = \frac{\omega_1}{\dot{\varepsilon}_e}, \quad \sigma^{fx} = \sigma_0 + \sigma_1\left[1 - \exp\left(-\left(\frac{\omega_1}{t_D\dot{\varepsilon}_e}\right)^n\right)\right] + \sigma_D\left(\frac{\dot{\varepsilon}_e}{\dot{\varepsilon}_0}\right)^{1/m}. \tag{7.51}$$

Let us note that the ageing time component of the fixed point is just the waiting time of dislocations defined in (7.6).

To study the behavior of the prototypical autonomous system (7.50), we linearize the system around its equilibrium point. Let $(\delta\sigma, \delta t_a)$ be the components of a small disturbance of the fixed point. One shows that the disturbance evolves according to

$$\frac{\mathrm{d}}{\mathrm{d}\varepsilon}\begin{bmatrix}\delta\sigma \\ \delta t_a\end{bmatrix} = \begin{bmatrix}\frac{\partial f}{\partial\sigma} & \frac{\partial f}{\partial t_a} \\ \frac{\partial g}{\partial\sigma} & \frac{\partial g}{\partial t_a}\end{bmatrix}_{\left(\sigma^{fx}, t_a^{fx}\right)}\begin{bmatrix}\delta\sigma \\ \delta t_a\end{bmatrix} + \text{quadratic terms.} \tag{7.52}$$

The matrix of this linearized system is called the Jacobian matrix at the fixed point. The type and the stability of the equilibrium points depends on the eigenvalues λ_1 and λ_2 of the Jacobian matrix and can be characterized through the values

of its trace, determinant and discriminant of the characteristic equation, (see for instance Strogatz 1994) i.e.

$$\begin{aligned}
\mathrm{Tr} = \lambda_1 + \lambda_2 &= -\frac{1}{\omega_1} - \frac{m}{\sigma_D}\left(\frac{\dot{\varepsilon}_0}{\dot{\varepsilon}_e}\right)^{1/m}\left[E - \frac{n\sigma_1}{\omega_1}\left(\frac{\omega_1}{t_D\dot{\varepsilon}_e}\right)^n \exp\left(-\left(\frac{\omega_1}{t_D\dot{\varepsilon}_e}\right)^n\right)\right], \\
\mathrm{Det} = \lambda_1\lambda_2 &= \frac{mE}{\sigma_D\omega_1}\left(\frac{\dot{\varepsilon}_0}{\dot{\varepsilon}_e}\right)^{1/m}, \\
\Delta = (\lambda_1 + \lambda_2)^2 - 4\lambda_1\lambda_2 &= \Delta(\dot{\varepsilon}_e, \dot{\varepsilon}_0, \sigma_1, \sigma_0, \omega_1, t_D, \sigma_D, E, n, m).
\end{aligned} \tag{7.53}$$

The positive value of the determinant rules out the possibility of having a saddle point. Hence the stability of the fixed point can be established just by looking at the sign of trace. Therefore, the equilibrium point can be only

- a *stable node* if $\mathrm{Tr} < 0$ and $\Delta > 0$,
- a *stable focus* if $\mathrm{Tr} < 0$ and $\Delta < 0$,
- an *unstable focus* if $\mathrm{Tr} > 0$ and $\Delta < 0$,
- an *unstable node* if $\mathrm{Tr} > 0$ and $\Delta > 0$.

In this case the linearized system gives a qualitatively correct picture of the phase portrait near the equilibrium point (σ^{fx}, t_a^{fx}). Usually, if the phase portrait changes its topological structure as a parameter is varied, one says that a *bifurcation* occurs. From $(7.53)_3$ one sees that the phase portrait depends on the following 10 mechanical parameters which correspond to:

- boundary condition (7.45): $\dot{\varepsilon}_e$,
- kinetic parameters of viscoplastic constitutive Eq. (7.20): $\dot{\varepsilon}_0$, σ_D, m,
- McCormick's law (7.25) and flow stress due to ageing (7.23): ω_1, σ_1, t_D, n,
- flow stress due to plastic deformation (7.22): σ_0.
- elastic Young modulus E.

We consider, for instance, that only the *characteristic strain-rate factor* $\dot{\varepsilon}_0$, (or, equivalently the *characteristic time* of the viscoplastic constitutive equation $\tau = 1/\dot{\varepsilon}_0$) and the *engineering strain-rate* $\dot{\varepsilon}_e$ vary, while the other parameters are fixed. Then, the corresponding bifurcation plane, is characterized by the curves across which the trace Tr and the discriminant Δ change their signs (see Fig. 7.18).

We show that instability phenomena for the autonomous system (7.50) can occur if and only if the mechanical parameters satisfy the following condition

$$A \equiv \frac{n\sigma_1}{\omega_1 E} > e, \tag{7.54}$$

where e is Euler's number.

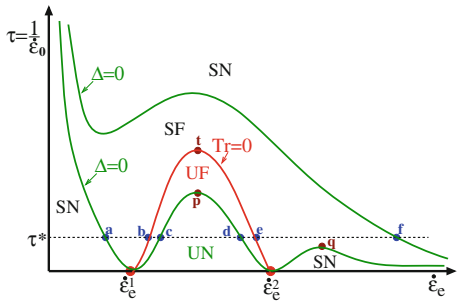

Fig. 7.18 Case $A > e$. Plane of bifurcation of the fixed point (7.51) corresponding to parameters $\tau = 1/\dot{\varepsilon}_0$ and $\dot{\varepsilon}_e$. SN stable node region ($\mathrm{Tr} < 0$, $\Delta > 0$); SF stable focus region ($\mathrm{Tr} < 0$, $\Delta < 0$); UF unstable focus region ($\mathrm{Tr} > 0$, $\Delta < 0$); UN unstable node region ($\mathrm{Tr} > 0$, $\Delta > 0$)

The fulfillment of this relation will also explain the existence of serrated curves for the non-homogeneous case considered in Sect. 7.3.3, i.e. for the strain-controlled initial-boundary value problems (7.42) for the PDEs system (7.41) (see Fig. 7.13).

To prove this statement let us introduce the notations

$$B \equiv \frac{m\omega_1 E}{\sigma_D}, \quad Z(\dot{\varepsilon}_e) \equiv \left(\frac{\omega_1}{t_D \dot{\varepsilon}_e}\right)^n. \tag{7.55}$$

First of all, observe that, if $A \leq e$, then $1 - Azexp(-z) \geq 0$, for any $z > 0$, and consequently, from $(7.53)_1$, it follows that $\mathrm{Tr}\,(\dot{\varepsilon}_0, \dot{\varepsilon}_e) \leq 0$, for any $\dot{\varepsilon}_0 > 0$ and $\dot{\varepsilon}_e > 0$. Therefore, in this case a fixed point can not be unstable.

If $A > e$, then $\mathrm{Tr}(\dot{\varepsilon}_0, \dot{\varepsilon}_e) > 0$ if and only if $0 < \tau = \frac{1}{\dot{\varepsilon}_0} < \tau_{tr}(\dot{\varepsilon}_e)$, where

$$\tau_{tr}(\dot{\varepsilon}_e) = \frac{1}{\dot{\varepsilon}_e} B^m [AZ(\dot{\varepsilon}_e) \exp(-Z(\dot{\varepsilon}_e)) - 1]^m, \quad \text{for } \dot{\varepsilon}_e \in \left(\dot{\varepsilon}_e^1, \dot{\varepsilon}_e^2\right), \tag{7.56}$$

and

$$\dot{\varepsilon}_e^1 = \dot{\varepsilon}_e^1(A, \omega_1, t_D) = \frac{\omega_1}{t_D (x_1)^{1/n}} < \frac{\omega_1}{t_D} < \dot{\varepsilon}_e^2 = \dot{\varepsilon}_e^2(A, \omega_1, t_D) = \frac{\omega_1}{t_D (x_2)^{1/n}}. \tag{7.57}$$

Here x_1, x_2 are the two solutions of the transcendental equation $exp(x) = Ax$ with the property that $x_2(A) < 1 < x_1(A)$.

An approximative solution of this equation, obtained using Newton's method, is

$$x_1 \cong \frac{(1 - A)\exp(1/A)}{A(\exp(1/A) - A)}, \quad x_2 \cong \frac{\sqrt{A}}{\sqrt{A} - 1}\left(3 \ln\left(\sqrt{A} - A\right)\right). \tag{7.58}$$

thus,

$$\dot{\varepsilon}_e^1 \cong \frac{\omega_1}{t_D}\left(\frac{\sqrt{A}-1}{\sqrt{A}(3\ln\sqrt{A}-1)}\right)^{1/n}, \quad \dot{\varepsilon}_e^2 \cong \frac{\omega_1}{t_D}\left(\frac{A(\exp(1/A)-A)}{\exp(1/A)(1-A)}\right)^{1/n}. \tag{7.59}$$

Thus, for $A > e$, $\tau = \tau_{tr}(\dot{\varepsilon}_e)$, is the unique positive curve in the bifurcation plane across which the trace changes its sign, i.e. across which the fixed point (7.51) switches from stable to unstable (see Fig. 7.18). $\dot{\varepsilon}_e^1$ and $\dot{\varepsilon}_e^2$ denote the intersection points of this curve with the axis $\tau = 0$. Therefore, the interval $(\dot{\varepsilon}_e^1, \dot{\varepsilon}_e^2)$ represents the maximal interval for the applied strain-rate $\dot{\varepsilon}_e$ in which a temporal instability can appear when $\dot{\varepsilon}_0 \to \infty$. Formulas (7.59) may give a direct hint about the way the mechanical parameters influence the range of the imposed engineering strain-rate $\dot{\varepsilon}_e$ for which a jerky flow can occur.

Furthermore, one can show that

$$\frac{\partial\dot{\varepsilon}_1^e}{\partial A}<0 \text{ and} \frac{\partial\dot{\varepsilon}_2^e}{\partial A}>0, \quad \frac{\partial\dot{\varepsilon}_1^e}{\partial\omega_1}>0 \text{ and} \frac{\partial\dot{\varepsilon}_2^e}{\partial\omega_1}<0, \quad \frac{\partial\dot{\varepsilon}_1^e}{\partial t_D}<0 \text{ and} \frac{\partial\dot{\varepsilon}_2^e}{\partial t_D}<0, \tag{7.60}$$

which lead to the following conclusions.

Remark 1 If the parameter A, $A > e$, increases, then the interval $(\dot{\varepsilon}_e^1, \dot{\varepsilon}_e^2)$ expands, while in the opposite case shrinks.

Remark 2 If the parameter ω_1 increases, then the interval $(\dot{\varepsilon}_e^1, \dot{\varepsilon}_e^2)$ shrinks, while in the opposite case expands.

Remark 3 If the parameter t_D decreases both the values of $\dot{\varepsilon}_e^1$ and $\dot{\varepsilon}_e^2$ increase.

The curve $\tau = \tau_{tr}(\dot{\varepsilon}_e)$ has a maximum at

$$\dot{\varepsilon}_e^3 = \dot{\varepsilon}_e^3(A,\omega_1,t_D,m,n) = \frac{\omega_1}{t_D(x_3)^{1/n}} \in \left(\frac{\omega_1}{t_D(1+1/m/n)^{1/n}}, \frac{\omega_1}{t_D}\right), \tag{7.61}$$

where x_3 is the solution of the equation $exp(x) = Ax(1+mn(1-x))$ in the interval (x_2, x_1) and $1<x_3<1+1/(mn)<x_1$. Indeed, this follows by analyzing its derivative,

$$\begin{aligned}\frac{\mathrm{d}\tau_{tr}(\dot{\varepsilon}_e)}{\mathrm{d}\dot{\varepsilon}_e} = \frac{B^m}{(\dot{\varepsilon}_e)^2}&[-1+AZ(\dot{\varepsilon}_e)\exp(-Z(\dot{\varepsilon}_e))]^{m-1}\\ &[1-AZ(\dot{\varepsilon}_e)(1+mn(1-Z(\dot{\varepsilon}_e)))\exp(-Z(\dot{\varepsilon}_e))].\end{aligned} \tag{7.62}$$

The maximum value at this point $\tau_{tr}^{max} = \tau_{tr}(\dot{\varepsilon}_e^3)$ determines the maximum value of the characteristic time τ, or equivalently, the minimum value of the characteristic strain-rate factor $\dot{\varepsilon}_0$ for which the fixed point (7.51) can become an *unstable focus*. This global maximum point is denoted by $\mathbf{t} = \mathbf{t}$ $(\dot{\varepsilon}_e^3, \tau_{tr}^{max})$ in Fig. 7.18.

Let us note that there are two positive curves across which the discriminant Δ change its sign, i.e. the eigenvalues change from real to complex (see Fig. 7.18). These are

$$\tau = \tau_{\Delta}^{\pm}(\dot{\varepsilon}_e) = \frac{1}{\dot{\varepsilon}_e} B^m \left(1 \pm \sqrt{AZ(\dot{\varepsilon}_e)\exp(-Z(\dot{\varepsilon}_e))}\right)^{2m}. \tag{7.63}$$

The graph of the function $\tau = \tau_{\Delta}^{-}(\dot{\varepsilon}_e)$ intersects the axis $\tau = 0$ at the points $\dot{\varepsilon}_e^1$ and $\dot{\varepsilon}_e^2$ defined by (7.57), where it reaches its minimum value. There are also two local maxima at the points

$$\dot{\varepsilon}_e^4 \equiv \frac{\omega_1}{t_D(x_4)^{1/n}} \in \left(\dot{\varepsilon}_e^3, \frac{\omega_1}{t_D}\right), \quad \text{and} \quad \dot{\varepsilon}_e^5 \equiv \frac{\omega_1}{t_D(x_5)^{1/n}} \in (\dot{\varepsilon}_e^2, \infty), \tag{7.64}$$

where x_5 and x_4 are the two solutions of the equation $exp(x) = Ax(1 + mn(1 - x))^2$, with the property that $x_5 \in (0, x_2)$ and $x_4 \in (1, x_3)$. Indeed, this follows by analyzing the expression of the derivative of this function, i.e.

$$\begin{aligned} \frac{\mathrm{d}\tau_{\Delta}^{-}(\dot{\varepsilon}_e)}{\mathrm{d}\dot{\varepsilon}_e} = \frac{B^m}{(\dot{\varepsilon}_e)^2}\left[-1 + \sqrt{AZ(\dot{\varepsilon}_e)\exp(-Z(\dot{\varepsilon}_e))}\right]^{2m-1} \\ \times \left[-1 + \sqrt{AZ(\dot{\varepsilon}_e)\exp(-Z(\dot{\varepsilon}_e))}(1 + mn(1 - Z(\dot{\varepsilon}_e)))\right]. \end{aligned} \tag{7.65}$$

The maximum value of the function τ_{Δ^-} at the point $\dot{\varepsilon}_e^4$ determines the maximum value of the characteristic time τ, or equivalently, the minimum value of the characteristic strain-rate factor $\dot{\varepsilon}_0$ for which the fixed point (7.51) can become an *unstable node*. These local maximum points are denoted by $\mathbf{p} = \mathbf{p}\left(\dot{\varepsilon}_e^4, \tau_{\Delta^-}(\dot{\varepsilon}_e^4)\right)$ and $\mathbf{q} = \mathbf{q}\left(\dot{\varepsilon}_e^5, \tau_{\Delta^-}(\dot{\varepsilon}_e^5)\right)$ in the bifurcation plane from Fig. 7.18.

7.4.2 Calibration of Mechanical Parameters

We analyze in the following the mechanical parameters of the model of dynamic strain ageing (DSA) presented in Sect. 7.2 and the way their values lead to the appearance of the PLC effect. Among these parameters we distinguish a first set, summarized in Table 7.1 which is related mainly to the classical elastic-viscoplastic approach used, and a second set, responsible for the evolution of the ageing time, i.e. of the DSA effect, which is shown in Table 7.2.

Material characterization and parameter identification from tension tests at a reference strain-rate for elastic-viscoplastic constitutive models of McCormick type has been considered, for instance, by Zhang et al. (2001) (for AlMgSi alloy), Benallal et al. (2008a) (for AA5083-H116 alloy plates), Böhlke et al. (2009) (for aluminium alloy 2024).

The term $\sigma_H(\varepsilon^p)$ which describes the effect of stress hardening associated with the dislocation density evolution in the stress flow (7.21) is given by a Voce-type equation in Zhang et al. (2001); Böhlke et al. (2009), by an extended Voce-rule in Benallal et al. (2008a, b) or by a power law in Zhang et al. (2012). This part of the constitutive approach does not influence the way the temporal instabilities related with the PLC effect manifests. We adopt here the same Voce-type equation as in Böhlke et al. (2009) (see Table 7.1), but we consider different values for the parameters m, σ_D and $\dot{\varepsilon}_0$. These latter quantities affect the stress component of the equilibrium point (7.51) and the kinetics of the viscoplastic processes in general. Only the elastic Young modulus E from Table 7.1, which is present in condition (7.54), influences the range of unstable PLC behavior.

The effect of DSA is accounted for by the additive term $\sigma_B(\varepsilon^p, t_a)$ in the flow stress, given by relation (7.23), and includes the material parameters t_D and n of the Cottrell-Bilby-Louat ageing kinetics. The maximum value of this contribution to the flow stress, i.e. $\sigma_1 + \varepsilon^p\sigma_2$, corresponds to the saturation of the local solute concentration on dislocations temporarily arrested at localized obstacles. This saturation value of the DSA related stress term is often considered constant (see Table 7.2). A linear plastic strain dependence has been introduced by Böhlke et al. (2009), instead of a plastic strain dependence introduced in the argument of the exponential function of the Cottrell-Bilby-Louat relation in Zhang et al. (2001).

Let us note that, parameter t_D, i.e. the characteristic time for solute diffusion across dislocations, intervenes only in formula of the stress component of the equilibrium point (7.51) and does not affect condition (7.54), that is, it does not influence the appearance of PLC effect. A discussion on how t_D is temperature dependent is done in Mesarovics (1995). We choose here for t_D the same value as in Böhlke et al. (2009).

According to the strain ageing kinetics proposed by Cottrell and Bilby (1949) the exponent n is 2/3. Starting with the paper by Springer and Schwink (1991) an exponent of $1/3$ has been used. Indeed, Ling and McCormick (1993) found that, for the Al-Mg-Si alloy, the exponent 1/3 is more appropriate to describe their results of strain-rate sensitivity measurements and this value is now accepted in the literature (see Table 7.2). Moreover, Ling et al. (1993) claim that the 1/3 value reflects pipe diffusion controlled strain ageing kinetics.

The evolution of the ageing time t_a in the DSA process is governed by the evolution Eq. (7.25) which includes essentially the material function $\Omega(\varepsilon^p) = \omega_1 + \varepsilon^p\omega_2$. Its value represents a strain increment produced when all arrested dislocations overcome localized obstacles and advance to the next pinned configuration. Mesarovics (1995) has evaluated by using the Orowan law (7.6) and some estimations of the densities of mobile and immobile dislocations that $\Omega \cong 10^{-4}$. The value of parameter Ω appears as essential in condition (7.54). Concerning the way Ω varies with the plastic strain Zhang et al. (2001) assumed the non-linear expression (7.7) while Böhlke et al. (2009) the linear one.

From Table 7.2 we see that for the mechanical parameters used by Zhang et al. (2001); Böhlke et al. (2009) condition (7.54) is not satisfied. Therefore, there is no

engineering strain-rate $\dot{\varepsilon}_e$ and no characteristic strain-rate factor $\dot{\varepsilon}_0$ for which the stress-strain curve of a homogeneous process, i.e. solution of the system (7.47), can be serrated. In other words, for these mechanical parameters the PLC effect can not occur. That is why, we used in this paper a larger value for σ_1, just as in Benallal et al. (2008a) and a lower value for ω_1, like in Zhang et al. (2001). With this choice condition (7.54) is fulfilled for $A = 8.23$ which is much larger than Euler's number e. We show in what follows how, under these circumstances, the unstable behavior specific for the PLC effect is captured.

We also notice that for the mechanical parameters used by Benallal et al. (2008a, b), Zhang et al. (2012) condition (7.54) is satisfied for a value of A slightly larger than e.

Further we illustrate how the stability/instability domains described by the curves (7.56) and (7.63) allow identification of the ranges of variation of the characteristic time $\tau = 1/\dot{\varepsilon}_0$ and of the engineering strain $\dot{\varepsilon}_e$ for which the PLC effect can appear. A similar bifurcation analysis can be done if one varies other material parameters of the model which are responsible for the PLC effect i.e., ω_1, t_D, σ_1, σ_D, m.

For the mechanical parameters in the fifth column in Tables 7.1 and 7.2 we have determined the main features of the bifurcation plane represented in Fig. 7.18 and we have summarized the corresponding results in Table 7.3.

Thus, if we choose the characteristic strain-rate factor $\dot{\varepsilon}_0^* = 3.5 \times 10^{-6}\ \mathrm{s}^{-1}$ then the intersection points of the horizontal line $\tau^* = 1/\dot{\varepsilon}_0^*$ with the curves which delimitate the domains of stability/unstability of the equilibrium point show that the range of the engineering strain-rate $\dot{\varepsilon}_e$ for which a jerky flow can appear is $(2.37 \times 10^{-5}\ \mathrm{s}^{-1}, 3.91 \times 10^{-3}\ \mathrm{s}^{-1})$. Indeed, this interval corresponds to the line segment (b, e) in Fig. 7.18 for which the fixed point is an unstable focus. This result is in agreement with the fact that the PLC effect can occur only for a range of engineering strain-rate and the numerical values obtained are appropriate to the ranges found experimentally.

According to the properties of the curves (7.56) and (7.63) in the bifurcation plane, if τ^* increases (i.e. $\dot{\varepsilon}_0^* = 1/\tau^*$ decreases), but without exceeding the value corresponding to the maximum point **t**, then the corresponding unstable focus interval for $\dot{\varepsilon}_e$ shrinks. For $\tau^* = 5.40 \times 10^9$ s (i.e. for $\dot{\varepsilon}_0^* = 1.85 \times 10^{-10}\ \mathrm{s}^{-1}$) the unstable interval reduces to the point $_e = 1.97 \times 10^{-4}\ \mathrm{s}^{-1}$.

If τ^* decreases (i.e., if $\dot{\varepsilon}_0^* = 1/\tau^*$ increases) then the corresponding interval of $\dot{\varepsilon}_e$ for which the fixed point is an unstable focus expands. The maximum interval is attained when $\tau^* \to 0$, that is $\dot{\varepsilon}_e \in \left(\dot{\varepsilon}_e^1 = 7.99 \times 10^{-6}\ \mathrm{s}^{-1}, \dot{\varepsilon}_e^2 = 1.05 \times 10^{-1}\ \mathrm{s}^{-1}\right)$ (see Table 7.3 and Fig. 7.18). Therefore, we can adjust the interval of the imposed strain-rate $\dot{\varepsilon}_e$ for which serrated curves appear with that found in laboratory tests for which the PLC effect manifests by an appropriate choice of the characteristic strain-rate factor $\dot{\varepsilon}_0$.

Moreover, the range of $\dot{\varepsilon}_e$ for which the equilibrium point (7.51) is an unstable point can be adapted, according to Remark 1–3 in Sect. 7.4.1, by increasing or decreasing the values of A, or ω_1, or t_D. We can also show that when m increases

Table 7.3 Type of equilibrium point (7.51) for parameters in Tables 7.1 and 7.2 and coordinates of the points in bifurcation plane from Fig. 7.18

Stability/Unstability intervals	Point on Fig. 7.18	$\dot{\varepsilon}_e\,(\mathrm{s}^{-1})$	$\tau\,(\mathrm{s})$	$\dot{\varepsilon}_0 = 1/\tau\,(\mathrm{s}^{-1})$
Stable node interval	$\uparrow$	$\uparrow$		
	a	5.99×10^{-7}	2.85×10^{5}	3.5×10^{-6}
Stable focus interval	$\downarrow$	$\downarrow$		
	$\dot{\varepsilon}_e^1$	7.99×10^{-6}	0	∞
Stable focus interval	$\uparrow$	$\uparrow$		
	b	2.37×10^{-5}	2.85×10^{5}	3.5×10^{-6}
Unstable focus interval	$\downarrow$	$\downarrow$		
	c	#	#	#
Unstable focus interval	$\updownarrow$	$\updownarrow$		
	t	1.97×10^{-4}	5.40×10^{9}	1.85×10^{-10}
Unstable focus interval	$\updownarrow$	$\updownarrow$		
	p	2.25×10^{-4}	14.93	6.69×10^{-2}
Unstable focus interval	$\updownarrow$	$\updownarrow$		
	d	#	#	#
Unstable focus interval	$\uparrow$	$\uparrow$		
	e	3.91×10^{-3}	2.85×10^{5}	3.5×10^{-6}
Stable focus interval	$\downarrow$	$\downarrow$		
	$\dot{\varepsilon}_e^2$	1.05×10^{-1}	0	∞
Stable focus interval	$\uparrow$	$\uparrow$		
	f	12.8	2.85×10^{5}	3.5×10^{-6}
Stable node interval	$\downarrow$	$\downarrow$		

There is no intersection between the graph of $\tau = \tau_{\Delta^-}(\dot{\varepsilon}_e)$ and $\tau^* = 1/\dot{\varepsilon}_0^* = 2.85 \times 10^5$ s

then the maximum values of the functions $\tau = \tau_{tr}(\dot{\varepsilon}_e)$ and $\tau = \tau_{\Delta^-}(\dot{\varepsilon}_e)$ attained at the points **t**, **p** and **q** increase.

In order to exemplify how the prediction of this bifurcation analysis is in agreement with the behavior of the solution of the autonomous nonlinear ODE system (7.50) we have considered for a fixed characteristic strain-rate factor $\dot{\varepsilon}_0^*$, or equivalently a fixed τ^* (see Table 7.3), different increasing values of the imposed strain-rate $\dot{\varepsilon}_e$, which covers in a successive manner the stable/unstable zones in Fig. 7.18.

If the pair $(\tau^*, \dot{\varepsilon}_e)$ lies in the *stable node region*, for instance below $\tau = \tau_{\Delta^-}(\dot{\varepsilon}_e)$, for $\dot{\varepsilon}_e < \dot{\varepsilon}_e^1$ (see Fig. 7.18) then the homogeneous solution in the viscoplastic domain is represented in Fig. 7.19. The process starts at the boundary between the elastic

and viscoplastic domain, i.e. the initial condition (σ, t_a) satisfies relations $\sigma = E\varepsilon = \sigma_0 + \sigma_1(1 - \exp(-(\varepsilon/\dot{\varepsilon}_e/t_D)^n)$ and $t_a = \varepsilon/\dot{\varepsilon}_e$.

One can see that there is no stress decay and the ageing time increases as long as the stress increases to its equilibrium value $\sigma_{eq}^{fx} = 211.5$ MPa, and afterwards the ageing time decays at the value of the waiting time $t_a^{fx} = \omega_1/\dot{\varepsilon}_e = 72$ s.

If the pair $(\tau^*, \dot{\varepsilon}_e)$ lies in the *stable focus area*, that is, between the points **a** and **b** in Fig. 7.18, then the homogeneous solution in the viscoplastic domain is illustrated in Fig. 7.20. One observes the appearance of a first stress decay followed by some small oscillations before to reach the equilibrium stress $\sigma_{eq}^{fx} = 214.4$ MPa. The ageing time behaves in the same manner, although the oscillations are not visible at the scale of the figure, and it stabilizes at the value of the waiting time $t_a^{fx} = \omega_1/\dot{\varepsilon}_e = 3.6$ s.

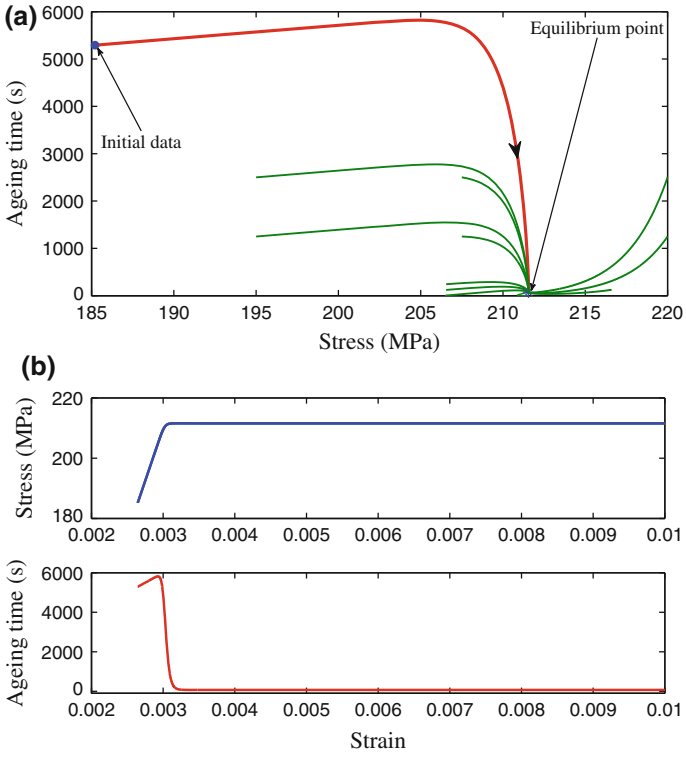

Fig. 7.19 *Stable Node Interval* $\dot{\varepsilon}_e = 5 \times 10^{-7}$ s^{-1} and $\dot{\varepsilon}_0^* = 3.5 \times 10^{-6}$ s^{-1} ($\tau^* = 2.85 \times 10^5$ s). Homogeneous process described by (7.50). **a** Phase portrait. **b** Stress and ageing time versus strain

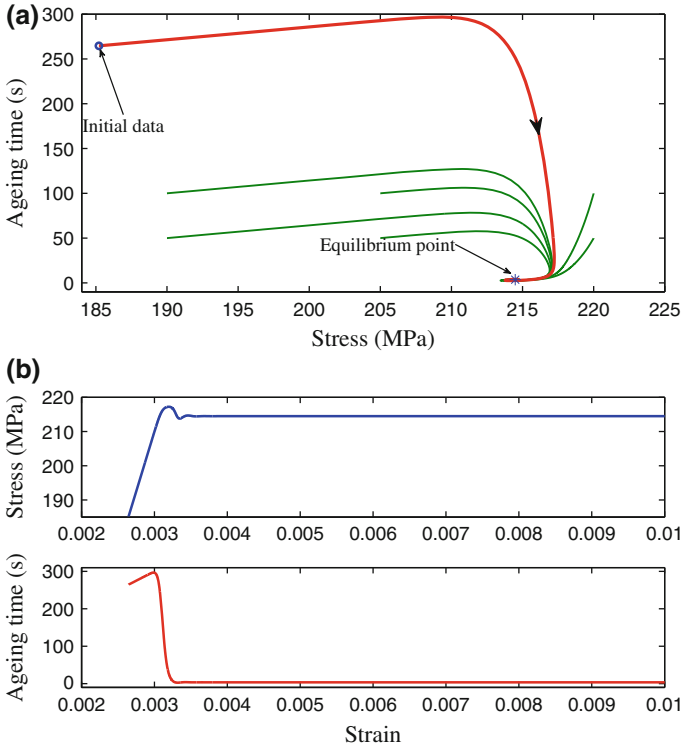

Fig. 7.20 *Stable Focus Interval* $\dot{\varepsilon}_e = 10^{-5}\ \mathrm{s}^{-1}$ and $\dot{\varepsilon}_0^* = 3.5 \times 10^{-6}\ \mathrm{s}^{-1}$ ($\tau^* = 2.85 \times 10^5$ s). Homogeneous process described by (7.50). **a** Phase portrait. **b** Stress and ageing time vs. strain

When the imposed strain-rate $\dot{\varepsilon}_e$ enters the estimated range of instability, that is, when the pair $(\tau^*, \dot{\varepsilon}_e)$ lies in the *unstable focus area* between the points **b** and **e** in Fig. 7.18, then the homogeneous solution in the viscoplastic domain is represented in Fig. 7.21. After a first drop of the stress and of the ageing time large oscillations, almost periodic, around the equilibrium point ($\sigma^{fx} = 196.8$ MPa, $t_a^{fx} = 0.036$ s) appear. The amplitude of the stress drop is around 23 MPa.

In this case the trajectories of the solutions in the phase plane spiral toward a *stable limit cycle*. This behavior illustrates that the nonlinear system is able to describe self-sustained oscillations. It is worth noting that the limit cycle shows a slow dynamics during one part of the cycle followed by a fast dynamics during the remaining part of the cycle. Indeed, one sees that the periodic oscillations consist of a slow increase of the stress which is followed by an abrupt fall in stress. This slow-fast dynamic process is in agreement with the characteristics of the PLC effect.

Oscillations of this type resemble with the so called "relaxation oscillations" of dynamical systems containing a small parameter which lead to singular perturbation. The prototype of this behavior is the van der Pol oscillator (see Strogatz 1994).

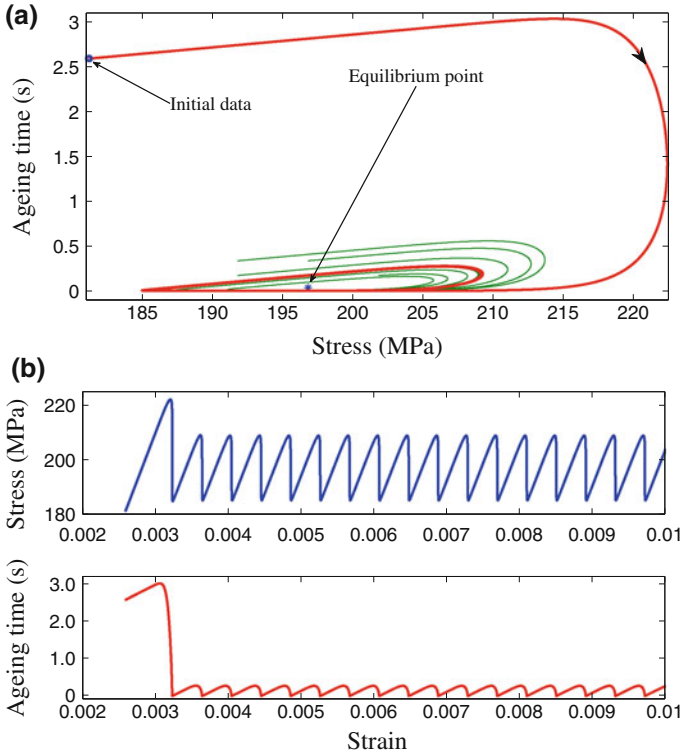

Fig. 7.21 *Unstable Focus Interval* $\dot{\varepsilon}_e = 10^{-3}\ \mathrm{s}^{-1}$ and $\dot{\varepsilon}_0^* = 3.5 \times 10^{-6}\ \mathrm{s}^{-1}$ ($\tau^* = 2.85 \times 10^5$ s). Homogeneous process described by (50). **a** Phase portrait. **b** Stress and ageing time vs. strain

Characteristic of the relaxation oscillations is the presence of phases in the cycle with different time scales: a phase of slow change followed by a short phase of rapid change in which the system practically jumps to the next stage of slow variation. In general, the specificity of these relaxation oscillations is that in a single period the solution describes two slow-fast alternation accompanied by two discontinuities, while for our nonlinear system (7.50) the solution experiences in a single period only one slow-fast alternation.

When, by increasing the imposed strain-rate, the pair $(\tau^*, \dot{\varepsilon}_e)$ enters again into a *stable focus region*, that is, it lies between the points **e** and **f** in Fig. 7.18, then the homogeneous process in the viscoplastic domain is represented in Fig. 7.22. The behavior of the solution is similar with that in Fig. 7.20, with the difference that the first stress drop is much more important and the oscillations are more visible before the solution reaches the equilibrium point ($\sigma^{fx} = 190.4$ MPa, $t_a^{fx} = 0.0036$ s).

We have also considered the case when the pair $(\tau, \dot{\varepsilon}_e)$ belongs to the *unstable node area*, that is, it lies below the curve $\tau = \tau_{\Delta^-}(\dot{\varepsilon}_e)$, for $\dot{\varepsilon}_e \in (\dot{\varepsilon}_e^1, \dot{\varepsilon}_e^2)$ in Fig. 7.18.

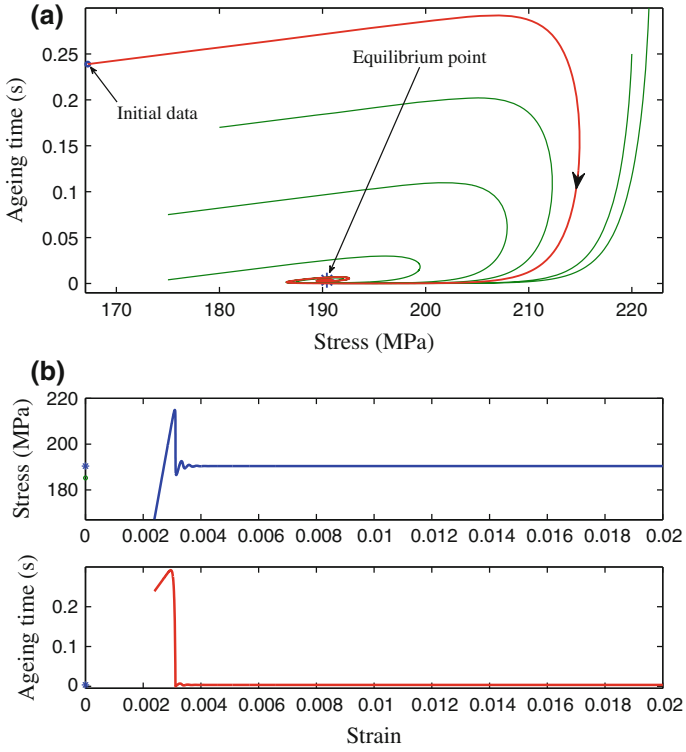

Fig. 7.22 *Stable Focus Interval* $\dot{\varepsilon}_e = 10^{-2}\ \mathrm{s}^{-1}$ and $\dot{\varepsilon}_0^* = 3.5 \times 10^{-6}\ \mathrm{s}^{-1}$ ($\tau^* = 2.85 \times 10^5$ s). Homogeneous process described by (7.50). **a** Phase portrait. **b** Stress and ageing time vs. strain

For instance, if we choose $\dot{\varepsilon}_e = 2.25 \times 10^{-4}\ \mathrm{s}^{-1}$, which corresponds to the local maximum point **p**, it follows that in order to be in the unstable area, according to Table 7.3, it is necessary that τ be less than 14.93 s, or equivalently $\dot{\varepsilon}_0$ be greater than $6.69 \times 10^{-2}\ \mathrm{s}^{-1}$. Such a situation is illustrated in Fig. 7.23. The same as in the case of the unstable focus fixed point the trajectories in the phase plane have the property that they approach a *stable limit cycle*. Numerical solutions illustrated in Fig. 7.23a show stable spirals giving rise to a limit cycle and to almost "periodic" oscillations. In this case both the stress and the ageing time show much larger oscillations around the equilibrium point ($\sigma^{fx} = 179.5$ MPa, $t_a^{fx} = 0.1636$ s). The amplitude of the stress drop increases to 50 MPa.

During a single period we record a slow and two fast variations of the solution. Indeed, the limit cycle consists of an extremely slow increase of the stress followed by a sudden discharge and a sudden rise of the stress. During the stress drop the ageing time reaches its minimum value, while it suffers a sudden increases during the sudden rise of the stress. This behavior is not typical to the PLC effect, but

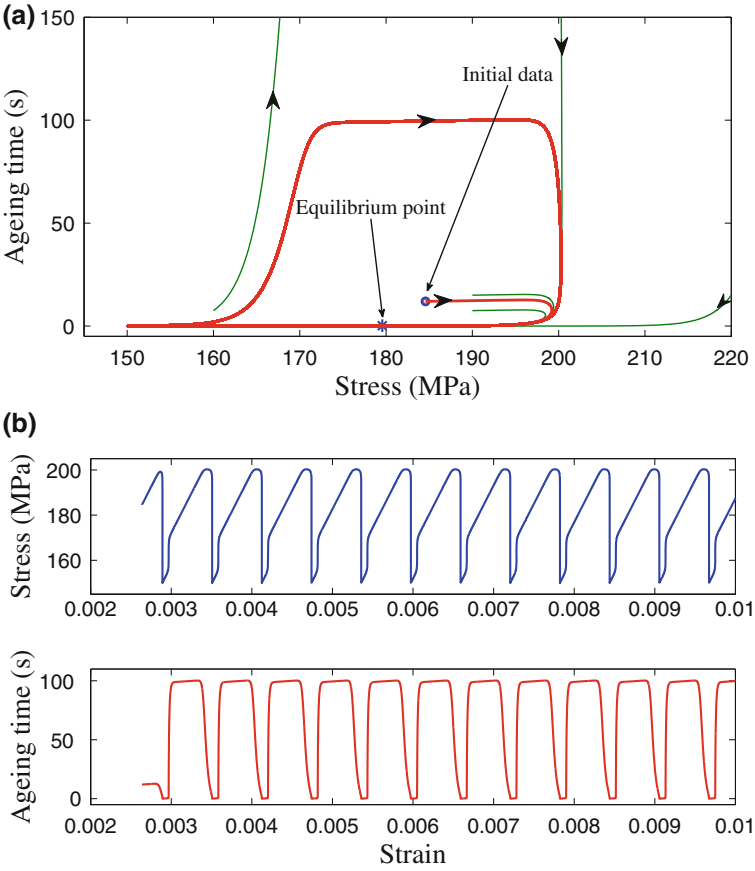

Fig. 7.23 *Unstable Node Area* $\dot{\varepsilon}_e = 2.2 \times 10^{-4}\ \mathrm{s}^{-1}$ and $\dot{\varepsilon}_0 = 6.\,\mathrm{s}^{-1}$ ($\tau = 0.16$ s). Homogeneous process described by (7.50). **a** Phase portrait. **b** Stress and ageing time vs. strain

illustrates how the nonlinear ODE system describes self-sustained oscillations for a large value of $\dot{\varepsilon}_0$.

The serrated stress-strain curves obtained in Figs. 7.21b and 7.23b show two important characteristic features: they are "horizontal" and have constant amplitude. The first is due to the fact that the strain hardening is neglected, while the second is a consequence of the assumption that the stress accounting for the PLC effect σ_B does not depend on ε^p, according to the constitutive relations (7.48) used in the bifurcation analysis.

Let us consider now the general case of the elastic-viscoplastic model with the strain hardening term $\sigma_H(\varepsilon^p)$ described by the Voce rule (7.22) and the term $\sigma_B(t_a, \varepsilon^p)$, responsible for the DSA effect, described by (7.23). The mechanical parameters are given in the fifth column in Tables 7.1 and 7.2.

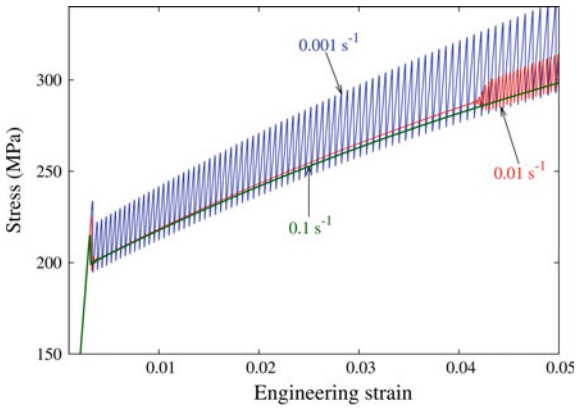

Fig. 7.24 Elastic-viscoplastic homogeneous process with strain hardening described by the non-autonomous system (7.47) for three imposed engineering strain-rates: $\dot{\varepsilon}_e = 10^{-3}\ \mathrm{s}^{-1}$, $\dot{\varepsilon}_e = 10^{-2}\ \mathrm{s}^{-1}$ and $\dot{\varepsilon}_e = 10^{-1}\ \mathrm{s}^{-1}$ when $\dot{\varepsilon}_0 = 3.5 \times 10^{-6}\ \mathrm{s}^{-1}$ ($\tau = 2.85 \times 10^5$ s)

In this case, the homogeneous process is described by the non-autonomous system (7.47) which includes both the elastic and the viscoplastic case. The numerical solutions obtained for three imposed engineering strain-rates $\dot{\varepsilon}_e$ are illustrated in Fig. 7.24.

The solution obtained for $\dot{\varepsilon}_e = 10^{-3}\ \mathrm{s}^{-1}$ has to be compared with the solution obtained in Fig. 7.21 when the fixed point is an unstable focus. One observes how the hardening rule leads to an increasing stress-strain serrated curve. Like in Fig. 7.21b there is an initial large stress drop, followed by large oscillations, but having now an increasing amplitude which ranges from 25.6 to 49.5 MPa. That is due to the fact that in the viscoplastic deformation process the term $\sigma_0 + \varepsilon^p \sigma_1$ which characterizes the saturation value of the DSA related stress term increases with plastic strain. This gradually increasing amplitude is in agreement with experimental facts (see for instance Fig. 7.1).

Moreover, it should be noted that a sawtooth is composed by a stress drop, which is a fast viscoplastic and dissipative process, while the reloading part, having the slope of the elastic Young modulus E, is a slow elastic process.

In the case of the higher strain-rate $\dot{\varepsilon}_e = 10^{-2}\ \mathrm{s}^{-1}$ the bifurcation analysis has predicted for the autonomous system, according to Fig. 7.22b, a stress-strain curve which is not serrated, since in this case we are outside the interval of instability described in Table 7.3. In the general case of the non-autonomous system (7.47) we see in Fig. 7.24 that the stress-strain curve preserves the same features as in the stable focus case for lower values of the engineering strain ε_e. Indeed, there is in the beginning a large stress drop followed by small oscillations which are damped and continued with a nice increasing smooth curve. If the strain becomes larger one can see that a serrated curve appears reflecting an unstable behavior of PLC type. This behavior is in agreement with the remarks in Sect. 7.4.1 that by increasing the value of the parameter $A = \frac{n\sigma_1}{\omega_1 E}$ the range of imposed strain-rate $\dot{\varepsilon}_e$ for which the

autonomous ODE system (7.50) has an unstable behavior expands. Indeed, in this case, if we consider the non-autonomous system (7.47) with frozen coefficients at ε^p then the parameter which characterizes the instability read as $A(\varepsilon^p) = \frac{n(\sigma_1 + \sigma_2 \varepsilon^p)}{\omega_1 E}$ and is increasing with the plastic strain. This explains the appearance of oscillations at this strain-rate for large value of the engineering strain ε_e.

If the strain-rate increases again by an order of magnitude, i.e. to 10^{-1}s^{-1}, one sees that the solution does not show unstable behavior for the range of strain in the figure, behavior which is in agreement with the stability/instability analysis.

Thus, the graphs obtained in Fig. 7.24 correspond to spatially homogeneous processes whose initial data are $(7.45)_1$ which is an ideal case since from the beginning we have supposed a linear distribution of the velocity in the bar. The real process corresponds to the initial-boundary value problem (7.42) which introduces from the start a small shock perturbation. This perturbation leads to spatial inhomogeneous solutions which have been analyzed in Sect. 7.3.3.1.

Therefore, the graphs in Fig. 7.24 have to be compared with those obtained in Fig. 7.13 for the non-homogeneous case. The similarities between the stress-strain curves confirm the bifurcation analysis performed and their differences highlight the influence of localization phenomena.

7.5 Conclusions and Outlook

The analyzed constitutive model for dynamic strain ageing provides a macroscopic description of the temporal and spatial features of the Portevin-Le Chatelier plastic instabilities in satisfactory agreement with experimental results. We have shown that, depending on the tensile testing conditions, the model describes both the serrated yielding and the staircase response. The sensitivity of the model to the boundary conditions can capture the influence of the testing machine on the stress - engineering strain curves as it is met in practice.

In order to improve the calibration of the mechanical parameters for critical conditions on PLC effect two directions require further analysis. The first one concerns the properties of the solutions of the autonomous dynamical system (7.50). We have seen that the appearance of a serrated stress-strain curve, i.e. of the unstable PLC behavior, is related to a Hopf bifurcation and that the emerging solution is a limit cycle in the phase plane. The shape and size of the limit cycle allows to estimate the amplitude of the periodic stress drops. But to find analytically the shape of the limit cycle for a dynamical system based on its equations is a tough problem. Therefore, in order to determine how the mechanical parameters of the model influence the serrations of a stress - strain curve one need to find a good estimate of a trapping region for the trajectories. That means to find a closed connected set in which all trajectories are confined (see Strogatz 1994).

A second direction is to investigate the influence of the parameters of the model on the localization phenomena which may develop in the dynamic strain ageing process. That means to perform a spatial stability analysis of the solutions of the

PDEs system (7.41). For doing this we have to analyze the stability of spatially homogeneous solutions to infinitesimal perturbations which is a necessary condition for the nucleation and propagation of strain bands.

Acknowledgments The author acknowledges support from the Romanian Ministry of Education and Research through Project PCCE ID-100/2010.

Appendix: Numerical Scheme

The numerical scheme used to solve the initial–boundary value problems (7.42)–(7.44) for the hyperbolic semilinear system of PDEs (7.41) is a variant of the standard method of characteristic (see for instance Mihăilescu-Suliciu and Suliciu 1985). A time integration step condition is used to ensure the numerical stability.

Let us note that by introducing the notations

$$p = \sigma + \sqrt{\rho E}v, \quad q = \sigma - \sqrt{\rho E}v, \quad r = \sigma - E\varepsilon, \tag{7.66}$$

we can write the system (7.41) in its characteristic form

$$\frac{\partial p}{\partial t} - C\frac{\partial p}{\partial X} = \tilde{G}(p,q,r,t_a), \quad \frac{\partial q}{\partial t} + C\frac{\partial q}{\partial X} = \tilde{G}(p,q,r,t_a), \tag{7.67}$$

$$\frac{\partial r}{\partial t} = \tilde{G}(p,q,r,t_a), \quad \frac{\partial t_a}{\partial t} = \tilde{H}(p,q,r,t_a), \tag{7.68}$$

where $C = \sqrt{E/\rho}$ is the longitudinal wave speed and

$$(\tilde{G},\tilde{H})(p,q,r,t_a) = (G,H)(\varepsilon,\sigma,t_a) = (G,H)\left(\frac{1}{E}\left(\frac{p+q}{2} - r\right), \frac{p+q}{2}, t_a\right).$$

Along the constant characteristic directions of the system the following relations are satisfied

$$\begin{aligned} \mathrm{d}p &= \tilde{G}(p,q,r,t_a)\mathrm{d}t \quad \text{on} \quad \mathrm{d}X = -C\mathrm{d}t, \\ \mathrm{d}q &= \tilde{G}(p,q,r,t_a)\mathrm{d}t \quad \text{on} \quad \mathrm{d}X = C\mathrm{d}t, \\ \mathrm{d}r &= \tilde{G}(p,q,r,t_a)\mathrm{d}t \quad \text{on} \quad \mathrm{d}X = 0, \\ \mathrm{d}t_a &= \tilde{H}(p,q,r,t_a)\mathrm{d}t \quad \text{on} \quad \mathrm{d}X = 0. \end{aligned} \tag{7.69}$$

The numerical solution is build in agreement to the stencil in Fig. 7.25. We partition the domain in space using a mesh $X_0,\ldots, X_i,\ldots, X_N$ and in time using a mesh $t_0,\ldots, t_j,\ldots$. We assume a uniform partition both in space and in time, so the difference between two consecutive space points will be h and between two

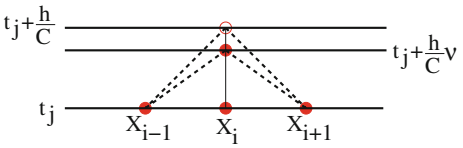

Fig. 7.25 Stencil for the method of characteristics

consecutive time points will be τ. We denote by $u(X_i, t_j) = u_i^j$ the values of a generic function u at the mesh points.

The *first order numerical approximation* is a set of four function (p, q, r, t_a) defined on the above mesh and satisfying the following iterative relations

$$\begin{aligned}
&\frac{p_i^{j+1} - p_i^j}{\tau} - \frac{C}{h}\left(p_{i+1}^j - p_i^j\right) = (1-\nu)\tilde{G}_i^j + \nu\tilde{G}_{i+1}^j,\\
&\frac{q_i^{j+1} - q_i^j}{\tau} + \frac{C}{h}\left(q_i^j - q_{i-1}^j\right) = (1-\nu)\tilde{G}_i^j + \nu\tilde{G}_{i-1}^j,\\
&r_i^{j+1} = r_i^j + \tau\tilde{G}_i^j, \quad t_{ai}^{j+1} = t_{ai}^j + \tau\tilde{H}_i^j,
\end{aligned} \tag{7.70}$$

where the Courant number ν has to satisfy condition

$$\nu \equiv C\frac{\tau}{h} \leq 1, \tag{7.71}$$

in order to ensure the numerical stability of the scheme (see Richtmyer and Morton 1967).

The iterative relations for this explicit scheme can be written as

$$\begin{aligned}
p_i^{j+1} &= (1-\nu)\left(p_i^j + \tau\tilde{G}_i^j\right) + \nu\left(p_{i+1}^j + \tau\tilde{G}_{i+1}^j\right),\\
q_i^{j+1} &= (1-\nu)\left(q_i^j + \tau\tilde{G}_i^j\right) + \nu\left(q_{i-1}^j + \tau\tilde{G}_{i-1}^j\right),\\
r_i^{j+1} &= r_i^j + \tau\tilde{G}_i^j, \quad t_{ai}^{j+1} = t_{ai}^j + \tau\tilde{H}_i^j,
\end{aligned} \tag{7.72}$$

or in terms of initial variables σ, ε, v, t_a the *first approximation* becomes

$$\begin{aligned}
\sigma_i^{j+1} &= (1-\nu)\sigma_i^j + \frac{\nu}{2}\left(\sigma_{i+1}^j + \sigma_{i-1}^j\right) + \frac{\nu}{2}\sqrt{\rho E}\left(v_{i+1}^j - v_{i-1}^j\right)\\
&\quad + \tau\left((1-\nu)G_i^j + \frac{\nu}{2}\left(G_{i+1}^j + G_i^j\right)\right),\\
v_i^{j+1} &= (1-\nu)v_i^j + \frac{\nu}{2}\left(v_{i+1}^j + v_{i-1}^j\right) + \frac{\nu}{2}\frac{1}{\sqrt{\rho E}}\left(\sigma_{i+1}^j - \sigma_{i-1}^j\right)\\
&\quad + \tau\frac{\nu}{2}\frac{1}{\sqrt{\rho E}}\left(G_{i+1}^j - G_{i-1}^j\right),\\
\varepsilon_i^{j+1} &= \varepsilon_i^j + \frac{1}{E}\left(\sigma_i^{j+1} - \sigma_i^j\right) - \tau\frac{1}{E}G_i^j, \quad t_{ai}^{j+1} = t_{ai}^j + \tau H_i^j.
\end{aligned} \tag{7.73}$$

The *second order numerical approximation* is a set of four function $\left(\overset{(2)}{p}, \overset{(2)}{q}, \overset{(2)}{r}, \overset{(2)}{t_a}\right)$ defined on the mesh and satisfying the following iterative relations

$$\begin{aligned}
&\frac{\overset{(2)}{p}{}_i^{j+1} - p_i^j}{\tau} - \frac{C}{h}\left(p_{i+1}^j - p_i^j\right) = \frac{(1-\nu)}{2}\left(\tilde{G}_i^j + \overset{(1)}{G}{}_i^{j+1}\right) + \frac{\nu}{2}\left(\tilde{G}_{i+1}^j + \overset{(1)}{G}{}_i^{j+1}\right),\\
&\frac{\overset{(2)}{q}{}_i^{j+1} - q_i^j}{\tau} + \frac{C}{h}\left(q_i^j - q_{i-1}^j\right) = \frac{(1-\nu)}{2}\left(\tilde{G}_i^j + \overset{(1)}{G}{}_i^{j+1}\right) + \frac{\nu}{2}\left(\tilde{G}_{i-1}^j + \overset{(1)}{G}{}_i^{j+1}\right),\\
&\overset{(2)}{r}{}_i^{j+1} = r_i^j + \frac{\tau}{2}\left(\tilde{G}_i^j + \overset{(1)}{G}{}_i^{j+1}\right), \quad \overset{(2)}{t_a}{}_i^{j+1} = t_{ai}^j + \frac{\tau}{2}\left(\tilde{H}_i^j + \overset{(1)}{H}{}_i^{j+1}\right),
\end{aligned} \tag{7.74}$$

where $\overset{(1)}{G}{}_i^{j+1} = \tilde{G}(p_i^{j+1}, q_i^{j+1}, r_i^{j+1}, t_{ai}^{j+1})$ and $\overset{(1)}{H}{}_i^{j+1} = \tilde{H}\left(p_i^{j+1}, q_i^{j+1}, r_i^{j+1}, t_{ai}^{j+1}\right)$ are computed using the first approximation (7.72).

The *second order numerical approximation* in terms of initial variables σ, ε, v, t_a becomes

$$\begin{aligned}
\overset{(2)}{\sigma}{}_i^{j+1} &= (1-\nu)\left(\sigma_i^j + \frac{\tau}{2}\left(G_i^j + \overset{(1)}{G}{}_i^{j+1}\right)\right) + \frac{\nu}{2}\left(\sigma_{i+1}^j + |\sigma_{i-1}^j\right) + \frac{\nu}{2}\sqrt{\rho E}\left(v_{i+1}^j - v_{i-1}^j\right)\\
&\quad + \nu\frac{\tau}{4}\left(2\overset{(1)}{G}{}_i^{j+1} + G_{i+1}^j + G_{i-1}^j\right),\\
\overset{(2)}{v}{}_i^{j+1} &= (1-\nu)v_i^j + \frac{\nu}{2}\left(v_{i+1}^j + v_{i-1}^j\right) + \frac{\nu}{2}\frac{1}{\sqrt{\rho E}}\left(\sigma_{i+1}^j - \sigma_{i-1}^j\right)\\
&\quad + \nu\frac{\tau}{4}\frac{1}{\sqrt{\rho E}}\left(G_{i+1}^j - G_{i-1}^j\right),\\
\overset{(2)}{\varepsilon}{}_i^{j+1} &= \varepsilon_i^j + \frac{1}{E}\left(\overset{(2)}{\sigma}{}_i^{j+1} - \sigma_i^j\right) - \frac{\tau}{2E}\left(G_i^j + \overset{(1)}{G}{}_i^{j+1}\right),\\
\overset{(2)}{t_a}{}_i^{j+1} &= t_{ai}^j + \frac{\tau}{2}\left(H_i^j + \overset{(1)}{H}{}_i^{j+1}\right),
\end{aligned} \tag{7.75}$$

where $\overset{(1)}{G}{}_i^{j+1} = G\left(\varepsilon_i^{j+1}, \sigma_i^{j+1}, t_{ai}^{j+1}\right)$ and $\overset{(1)}{H}{}_i^{j+1} = H\left(\varepsilon_i^{j+1}, \sigma_i^{j+1}, t_{ai}^{j+1}\right)$ are computed using the first approximation (7.73).

Boundary conditions

The *left boundary condition* $v(0,t) = V^*$, or equivalently, $p(0,t) - q(0,t) = 2\sqrt{\rho E}V^*$, for the *strain controlled experiment* (7.42), leads to the following iterative relations.

The *first order approximation* at the node X_0 read as

$$\begin{aligned}
\sigma_0^{j+1} &= (1-\nu)\left(\sigma_0^j + \sqrt{\rho E}V^* + \tau G_0^j\right) + \nu\left(\sigma_1^j + \sqrt{\rho E}v_1^j + \tau G_1^j\right) - \sqrt{\rho E}V^*,\\
v_0^{j+1} &= V^*,\\
\varepsilon_0^{j+1} &= \varepsilon_0^j + \frac{1}{E}\left(\sigma_0^{j+1} - \sigma_0^j\right) - \frac{\tau}{E}G_0^j, \quad t_{a0}^{j+1} = t_{a0}^j + \tau H_0^j.
\end{aligned} \tag{7.76}$$

and the *second order approximation* is

$$\begin{aligned}
\overset{(2)}{\sigma}{}_0^{j+1} &= (1-\nu)\left(\sigma_0^j + \sqrt{\rho E}V^* + \frac{\tau}{2}\left(\overset{(1)}{G}{}_0^{j+1} + G_0^j\right)\right)\\
&\quad + \nu\left(\sigma_1^j + \sqrt{\rho E}v_1^j + \frac{\tau}{2}\left(\overset{(1)}{G}{}_0^{j+1} + G_1^j\right)\right) - \sqrt{\rho E}V^*,\\
\overset{(2)}{v}{}_0^{j+1} &= V^*,\\
\overset{(2)}{\varepsilon}{}_0^{j+1} &= \varepsilon_0^j + \frac{1}{E}\left(\overset{(2)}{\sigma}{}_0^{j+1} - \sigma_0^j\right) - \frac{\tau}{2E}\left(G_0^j + \overset{(1)}{G}{}_0^{j+1}\right), \quad \overset{(2)}{t}{}_{a0}^{j+1} = t_{a0}^j + \frac{\tau}{2}\left(H_0^j + \overset{(1)}{H}{}_0^{j+1}\right).
\end{aligned} \tag{7.77}$$

where $\overset{(1)}{G}{}_0^{j+1} = G\left(\varepsilon_0^{j+1}, \sigma_0^{j+1}, t_{a0}^{j+1}\right)$ and $\overset{(1)}{H}{}_0^{j+1} = H\left(\varepsilon_0^{j+1}, \sigma_0^{j+1}, t_{a0}^{j+1}\right)$ are computed using the first approximation given by relations (7.76).

The *left boundary condition* $\sigma(0,t) = S^*(t)$, or equivalently, $p(0,t) + q(0,t) = 2S^*(t)$, for the *stress controlled experiment* (7.42), leads to the following iterative relations.

The *first order approximation* at the node X_0 read as

$$\begin{aligned}
\sigma_0^{j+1} &= S^*((j+1)\tau),\\
v_0^{j+1} &= (1-\nu)\left(v_0^j + \frac{S^*(j\tau)}{\sqrt{\rho E}} + \frac{\tau}{\sqrt{\rho E}}G_0^j\right)\\
&\quad + \nu\left(v_1^j + \frac{\sigma_1^j}{\sqrt{\rho E}} + \frac{\tau}{\sqrt{\rho E}}G_1^j\right) - \frac{S^*((j+1)\tau)}{\sqrt{\rho E}},\\
\varepsilon_0^{j+1} &= \varepsilon_0^j + \frac{1}{E}\left(\sigma_0^{j+1} - \sigma_0^j\right) - \frac{\tau}{E}G_0^j, \quad t_{a0}^{j+1} = t_{a0}^j + \tau H_0^j.
\end{aligned} \tag{7.78}$$

and the *second order approximation* is

$$
\begin{aligned}
&{}^{(2)}\sigma_0^{j+1} = S^*((j+1)\tau)\\
&{}^{(2)}v_0^{j+1} = (1-v)\left(v_0^j + \frac{S^*(j\tau)}{\sqrt{\rho E}} + \frac{\tau}{2\sqrt{\rho E}}\left(G_0^j + {}^{(1)}G_0^{j+1}\right)\right)\\
&\qquad + v\left(v_1^j + \frac{\sigma_1^j}{\sqrt{\rho E}} + \frac{\tau}{2\sqrt{\rho E}}\left(G_1^j + {}^{(1)}G_0^{j+1}\right)\right) - \frac{S^*((j+1)\tau)}{\sqrt{\rho E}},\\
&{}^{(2)}\varepsilon_0^{j+1} = \varepsilon_0^j + \frac{1}{E}\left({}^{(2)}\sigma_0 j+1 - \sigma_0^j\right) - \frac{\tau}{2E}\left(G_0^j + {}^{(1)}G_0^{j+1}\right), \quad {}^{(2)}t_{a\,0}^{j+1} = t_{a\,0}^j + \frac{\tau}{2}\left(H_0^j + {}^{(1)}H_0^{j+1}\right).
\end{aligned}
\tag{7.79}
$$

where ${}^{(1)}G_0^{j+1} = G\left(\varepsilon_0^{j+1}, \sigma_0^{j+1}, t_{a\,0}^{j+1}\right)$ and ${}^{(1)}H_0^{j+1} = H\left(\varepsilon_0^{j+1}, \sigma_0^{j+1}, t_{a\,0}^{j+1}\right)$ are computed using the first approximation given by relations (7.78).

References

Ait-Amokhtar H, Fressengeas C, Boudrahema S (2008) The dynamics of Portevin-Le Chatelier bands in an Al-Mg alloy from infrared thermography. Mat Sci Eng A-Struct 488:540–546

Ait-Amokhtar H, Fressengeas C (2010) Crossover from continuous to discontinuous propagation in the Portevin–Le Chatelier effect. Acta Mater 58:1342–1349

Bell JF (1973) Handbuch der Physik, Band VIa/I. Springer Verlag, Berlin, pp. 649–666

Benallal A, Børvik T, Clausen AH, Hopperstad OS (2003) Dynamic strain aging, negative strain-rate sensitivity and related instabilities. Tech Mech 23:160–166

Benallal A, Berstad T, Børvik T, Clausen AH, Hopperstad OS (2006) Dynamic strain aging and related instabilities: experimental, theoretical and numerical aspects. Eur J Mech A-Solid 25:397–424

Benallal A, Berstad T, Børvik T, Hopperstad OS, Koutiri I, de Nogueira Codes R (2008a) An experimental and numerical investigation of the behaviour of AA5083 aluminium alloy in presence of the Portevin–Le Chatelier effect. Int J Plast 24:1916–1945

Benallal A, Berstad T, de Nogueira Codes R, Børvik T, Hopperstad OS (2008b) Effects of strain rate on the characteristics of PLC deformation bands for AA5083-H116 aluminium alloy. Philos Mag 88:3311–3338

Böhlke T, Bondár G, Estrin Y, Lebyodkin MA (2009) Geometrically non-linear modeling of the Portevin-Le Chatelier effect. Comput Mat Sci 44:1076–1088

Chihab K, Estrin Y, Kubin LP, Vergnol J (1987) The kinetics of the Portevin-Le Chatelier bands in an Al-5at%Mg alloy. Scripta Metall Mater 21:203–208

Chmelík F, Klose FB, Dierke H, Šachl J, Neuhäuser H, Lukáč P (2007) Investigating the Portevin-Le Châtelier effect in strain rate and stress rate controlled tests by the acoustic emission and laser extensometry techniques. Mat Sci Eng A-Struct 462:53–60

Cottrell AH, Bilby B (1949) Dislocation theory of yielding and strain ageing of iron. Proc Phys Soc Lon Sect A 62:49–62

Cottrell AH (1953) Dislocations and plastic flow in crystals. Oxford University Press, Oxford

Cristescu N, Suliciu I (1982) Viscoplasticity. Martinus Nijhoff Publishers, Bucharest

Cuddy LJ, Leslie WC (1972) Some aspects of serrated yielding in substitutional solid solutions of iron. Acta Metall Mater 20:1157–1167

Estrin Y (1996) Dislocation-density-related constitutive modeling. In: Krausz AS, Krausz K (eds) Unified constitutive laws of plastic deformation. Academic Press, San Diego

Făciu C (1998) A new rate-type gradient-dependent viscoplastic approach for "stop-and-go" strain band propagation. Numerical vs. physical experiments. J Phys IV Fr 8:143–150

Fellner M, Hamerský M, Pink E (1991) A comparison of the Portevin-Le Chatelier effect in constant-strain-rate and constant-stress-rate tests. Mat Sci Eng A-Struct 136:157–161
Graff S, Forest S, Strudel J-L, Prioul C, Pilvin P, Béchade J-L (2004) Strain localization phenomena associated with static and dynamic strain ageing in notched specimens: experiments and finite element simulations. Mat Sci Eng A-Struct 387–389:181–185
Halim H, Wilkinson DS, Niewczas M (2007) The Portevin-Le Chatelier (PLC) effect and shear band formation in an AA5754 alloy. Acta Mater 55:4151–4160
Hähner P (1993) Modelling the spatio-temporal aspects of the Portevin-Le Chatelier effect. Mat Sci Eng A-Struct 164:23–34
Jiang HF, Zhang QC, Chen XD, Chen ZG, Jiang ZY, Wu XP, Fan JH (2007) Three types of Portevin-Le Chatelier effects: experiment and modelling. Acta Mater 55:2219–2228
Kubin L, Estrin Y (1985) Portevin - Le Chatelier effect in deformation with constant stress rate. Acta Metall Mater 33:397–407
Ling CP, McCormick PG (1993) The effect of temperature on strain rate sensitivity in an Al-Mg-Si alloy. Acta Metall Mater 41:3127–3131
Ling CP, McCormick PG, Estrin Y (1993) A load perturbation method of examining dynamic strain ageing. Acta Metall Mater 41:3323–3330
Louat N (1981) On the theory of the Portevin-Le Chatelier effect. Scripta Metall Mater 15:1167–1170
Masson AP (1841) Sur l'élasticité des corpes solides. Ann Chim Phys (third series) 3:461–462
Mazière M, Dierke H (2012) Investigations on the Portevin-Le Chatelier critical strain in an aluminum alloy. Comput Mat Sci 52:68–72
McCormick PG (1988) Theory of flow localisation due to dynamic strain ageing. Acta Metall Mater 36:3061–3067
McCormick PG, Ling CP (1995) Numerical modelling of the Portevin-Le Chatelier effect. Acta Metall Mater 43:1969–1977
Mesarovics SDJ (1995) Dynamic strain aging and plastic instabilities. J Mech Phys Solids 43:671–700
Mihăilescu-Suliciu M, Suliciu I (1985) On the method of characteristics in rate-type viscoelasticity. ZAMM-Z Angew Math Mech 65:479–486
Mulford RA, Kocks UF (1979) New observations on the mechanisms of dynamic strain aging and of jerky flow. Acta Metall Mater 27:1125–1134
Nabarro FRN (1967) Theory of crystal dislocations. Clarendon Press, Oxford
Neuhäuser H, Klose FB, Hagemann F, Weidenmüller J, Dierke H, Hähner P (2004) On the PLC effect in strain-rate and stress-rate controlled tests-studies by laser scanning extensometry. J Alloy Compd 378:13–18
Picu RC (2004) A mechanism for the negative strain-rate sensitivity of dilute solid solutions. Acta Mater 52:3447–3458
Penning P (1972) Mathematics of the Portevin-Le Chatelier effect. Acta Metall Mater 20:1169–1175
Portevin A, Le Chatelier F (1923) Sur un phénomène observé lors de l'essai de traction d'alliages en cours de transformation. CR Acad Sci 176:507–510
Richtmyer RD, Morton KW (1967) Difference methods for initial-value problems. Wiley, New York
Rizzi E, Hähner P (2004) On the Portevin - Le Chatelier effect: theoretical modeling and numerical results. Int J Plast 20:121–165
Savart F (1837) Recherches sur les vibrations longitudinales. Ann Chim Phys (second series) 65:337–340
Scott VF, Mertens F, Marder M (2000) Portevin - Le Chatelier effect. Phys Rev E 6:8195–8206
Schwarz RB (1985) The Portevin-LeChatelier effect: I. model for the type-B serrations. In: McQueen HJ et al (ed) Proceedings of ICSMA 7, vol. 1. Pergamon Press, Toronto, pp. 343–348
Soare MA, Curtin WA (2008a) Solute strengthening of both mobile and forest dislocations: The origin of dynamic strain aging in fcc metals. Acta Mater 56:4046–4061

Soare MA, Curtin WA (2008b) Single-mechanism rate theory for dynamic strain aging in fcc metals. Acta Mater 56:4091–4101

Strogatz SH (1994) Nonlinear dynamics and chaos. Perseus Books Publishing, Reading

Springer F, Schwink Ch (1991) Quantitative investigations on dynamic strain ageing in polycrystalline CuMn alloys. Scr Metall Mater 25:2739–2744

Springer F, Nortmann A, Schwink Ch (1998) A study of basic processes characterizing dynamic strain ageing. Phys Status Solidi A 170:63–81

van den Beukel A (1975) Theory of the effect of dynamic strain aging on mechanical properties. Phys Status Solidi A 30:197–206

Yilmaz A (2011) The Portevin-Le Chatelier effect: a review of experimental findings. Sci Technol Adv Mater 12(063001):1–16

Zdunek J, Brynk T, Mizera J, Pakieła Z, Kurzydłowski KJ (2008) Digital image correlation investigation of Portevin-Le Chatelier effect in an aluminium alloy. Mater Charact 59:1429–1433

Zhang S, McCormick PG, Estrin Y (2001) The morphology of Portevin-Le Chatelier bands: finite element simulation for Al-Mg-Si. Acta Mater 49:1087–1094

Zhang F, Bower AF, Curtin WA (2012) The influence of serrated flow on necking in tensile specimens. Acta Mater 60:43–50